

# Measurement

## Emphasizing on the envelope spectra of hydraulic turbomachinery vibration response towards cavitation diagnosis --Manuscript Draft--

<b>Manuscript Number:</b>	MEAS-D-24-03652
<b>Article Type:</b>	Research Paper
<b>Keywords:</b>	Cavitation, Condition Based Maintenance, Pumps, Signal Processing, Vibration
<b>Corresponding Author:</b>	Georgios Mousmoulis, Ph.D. KU Leuven BELGIUM
<b>First Author:</b>	Georgios Mousmoulis
<b>Order of Authors:</b>	Georgios Mousmoulis Ioannis Anagnostopoulos George Aggidis Konstantinos Gryllias
<b>Abstract:</b>	<p>Cavitation attracts the interest of engineers who target the better understanding of its complex physics and the development of efficient detection tools. This research explores the effectiveness of vibration-based indicators in the prompt and effective diagnosis of cavitation initiating in the rotating flow fields of turbomachinery. The indicators are derived from the envelope spectra estimated with the use of Hilbert Transform, Spectral Kurtosis and Cyclic Spectral Correlation algorithms and data acquired from two semi-open impellers. By utilizing a transparent casing, the onset of cavitation can be observed, enabling the establishment of reliable criteria for evaluating the new indicators. Also, their applicability is assessed across a wide range of flow-rate and suction pressure conditions and in two different geometries. The results demonstrate the consistent ability of the indicators to exploit the high frequency carrier information related with the resonances excited from bubble implosions, to promptly and efficiently detect the phenomenon.</p>

To the Editors of Journal of Measurement:

Please consider the attached manuscript entitled “Emphasizing on the envelope spectra of hydraulic turbomachinery vibration response towards cavitation diagnosis” for possible publication in Journal of Measurement.

The paper assess the effectiveness of vibration-based indicators to promptly and accurately diagnose cavitation in hydraulic turbomachinery. The indicators are calculated based on envelope spectra obtained from Hilbert Transform, Spectral Kurtosis, and Cyclic Spectral Correlation algorithms. The latter are applied to vibration data collected from two semi-open impellers installed in a centrifugal pump with transparent casing that allows the visual observation of the phenomenon. The camera ground truth data are exploited towards the determination of the healthy condition threshold and the evaluation of the indicators cavitation detection effectiveness. The paper investigates the applicability of these indicators across a wide range of flow rates and suction pressure conditions, as well as in two different geometries. The results consistently demonstrate that Improved Envelope Spectrum-based indicators effectively leverage the high-frequency carrier information associated with resonances generated from bubble implosions, enabling prompt and efficient detection of the cavitation phenomenon.

Please let us know if this submittal meets your requirements for sending in manuscripts for possible review, and please feel free to contact us for anything else you may require.

Thank you for possibly considering this manuscript,

Dr.-Ing. Georgios Mousmoulis




- Influence of flowrate, NPSH and pump geometry on envelope spectra
- Use of Improved Envelope Spectrum (IES) for cavitation diagnosis purposes
- Evaluation of indicators based on effectiveness and robustness
- Exploit camera information for indicators evaluation

**Declaration of interests**

The authors declare that they have no known competing financial interests or personal relationships that could have appeared to influence the work reported in this paper.

The authors declare the following financial interests/personal relationships which may be considered as potential competing interests:

**We the undersigned agree with all of the above.**

Author's name (Fist, Last)	Signature	Date
1. Georgios Mousmoulis		28/03/2024
2. Ioannis Anagnostopoulos		28/03/2024
3. George Aggidis	 George A. Aggidis	28/03/2024

4. Konstantinos Gryllias

A handwritten signature in black ink, appearing to be 'Konstantinos Gryllias', written in a cursive style.

28/03/2024

# **Emphasizing on the envelope spectra of hydraulic turbomachinery vibration response towards cavitation diagnosis**

**Georgios Mousmoulis <sup>\*,1,2</sup>, Ioannis Anagnostopoulos <sup>3</sup>, George Aggidis <sup>4</sup>, Konstantinos Gryllias <sup>1,2</sup>**

\*Corresponding author: [georgios.mousmoulis@kuleuven.be](mailto:georgios.mousmoulis@kuleuven.be)

<sup>1</sup> KU Leuven, Department of Mechanical Engineering, Celestijnenlaan 300, B-3001, Heverlee, Belgium

<sup>2</sup> Flanders Make@KU Leuven, Belgium

<sup>3</sup> National Technical University of Athens, School of Mechanical Engineering, Iroon Polytechniou 9, 15780, Athens, Greece

<sup>4</sup> Lancaster University, School of Engineering, Gillow Ave, LA1 4YW, Lancaster, United Kingdom

# Emphasizing on the envelope spectra of hydraulic turbomachinery vibration response towards cavitation diagnosis

Georgios Mousmoulis <sup>\*1,2</sup>, Ioannis Anagnostopoulos <sup>3</sup>, George Aggidis <sup>4</sup>, Konstantinos Gryllias <sup>1,2</sup>

\*Corresponding author: [georgios.mousmoulis@kuleuven.be](mailto:georgios.mousmoulis@kuleuven.be)

<sup>1</sup> KU Leuven, Department of Mechanical Engineering, Celestijnenlaan 300, B-3001, Heverlee, Belgium

<sup>2</sup> Flanders Make@KU Leuven, Belgium

<sup>3</sup> National Technical University of Athens, School of Mechanical Engineering, Iroon Polytechniou 9, 15780, Athens, Greece

<sup>4</sup> Lancaster University, School of Engineering, Gillow Ave, LA1 4YW, Lancaster, United Kingdom

## Abstract

Cavitation attracts the interest of engineers who target the better understanding of its complex physics and the development of efficient detection tools. This research explores the effectiveness of vibration-based indicators in the prompt and effective diagnosis of cavitation initiating in the rotating flow fields of turbomachinery. The indicators are derived from the envelope spectra estimated with the use of Hilbert Transform, Spectral Kurtosis and Cyclic Spectral Correlation algorithms and data acquired from two semi-open impellers. By utilizing a transparent casing, the onset of cavitation can be observed, enabling the establishment of reliable criteria for evaluating the new indicators. Also, their applicability is assessed across a wide range of flow-rate and suction pressure conditions and in two different geometries. The results demonstrate the consistent ability of the indicators to exploit the high frequency carrier information related with the resonances excited from bubble implosions, to promptly and efficiently detect the phenomenon.

## 1. Introduction

Cavitation is the most common type of flow-related fault mechanism in machines that use liquid working mediums, i.e. from pumps to hydro-turbines and from propellers to internal combustion engines. The reliquification of the vapor bubbles that are formed due to the local drop of static pressure generates strong pressure waves that impinge the neighboring solid surfaces and reduce the machine efficiency [1], [2]. Moreover, in fluid machinery used for medical purposes (e.g. ventricular assist devices), cavitation initiation can also cause damage to the user's red blood cells [3], [4] resulting to serious hemolysis problems. Thus, in order to ensure the safe and efficient operation of fluid machinery, the prompt and robust diagnosis of cavitation with the use of modern condition based maintenance techniques is of paramount importance. The latter comprise transducers, acquisition devices and signal processing methodologies that target to sense and reveal the inherently dynamic vapor bubble implosions.

The sensors monitor either the actual pressure wave in the flow (i.e. pressure sensors and hydrophones) or the structural vibration (i.e. accelerometers) and the elastic waves (i.e. acoustic emission sensors) at the machine casing or the noise emitted from the machine (i.e. microphones) [5]. In addition, the signals acquired are usually processed in the time and frequency domain, where the indicators are formed based on the statistical properties (RMS, kurtosis etc.) of the timeseries [6]–[8] and the amplitudes of discrete or range of frequency components [9]–[16], respectively. In cases close to the phenomenon onset, where

bubbles exhibit transient behavior and do not appear steadily in the flow, the use of Short Time Fourier Transform (STFT) is implemented to reveal the appearance of excitations in the frequency domain in specific time instants [17], [18]. Although the aforementioned approaches have been proven very effective to detect the problematic operation of the machine (i.e. the symptom), they cannot provide additional diagnostic information about the failure type and its location in the system. For instance, many types of faults are expected to increase the vibration signal amplitude, resulting in an increase in the signal statistics (e.g. RMS, standard deviation etc.) [6], [7], while the majority of impulsive nature faults (e.g. cavitation and bearing related faults) give a rise in the kurtosis or in the high frequency resonances of the frequency spectrum [19]–[22].

An alternative to the traditional time and frequency approaches that can give more diagnostic insights, is the analysis of the modulations of the carriers (resonances) excited from the fault mechanism. The fault mechanism in the case of cavitation is the implosion of the vapor bubbles, when the latter pass to areas where pressure increases to values higher than the vapor pressure value. The high pressure intensity of the pressure waves generated during the bubble implosion can excite the machine structure resonances. To efficiently reveal the modulations from cavitation, the measured signal is filtered with the use of a band pass filter that its central frequency,  $f_c$  and bandwidth,  $bw$ , coincide with the position of the resonances (carriers). Then, the filtered signal is demodulated with the use of Hilbert Transform (HT) and the calculation of the Squared Envelope Spectrum (SES) [23], [24]. In studies performed in Francis turbines, the resonances excited from cavitation are identified by the analysis of the frequency spectrum and in two cases ([25], [26]) are located at  $f > 30$  kHz and in one case [16] at the high frequency side of the spectrum, with  $f = [3-6]$  kHz. In those results, the Envelope Spectrum (ES) can diagnose the type and position of the cavitation, since the cyclic modulations are related with the rotating flow field of the hydro-turbine. More specifically, in the case of vortex rope cavitation developed at the machine's outlet draft tube [16], [25], [27], the cyclic component exhibits a low value, usually close to the  $1/3$  of the shaft Rotational Frequency (RF), while in the case of cavitation initiation in the hydro-turbine runner or inlet casing, the Blade Passing Frequency (BPF) of the runner or the guide vanes appears in the ES.

The optimization of the selection strategy of the band pass filter characteristics that targets the identification of the resonance frequency areas excited from impulsive nature faults in rotating machinery is a very popular topic discussed from several authors [28]–[31]. The extraction of this information from the signal is achieved by the identification of the frequency content that includes the most non-stationary information. To measure the non-stationarity of the spectrum components, the kurtosis value is used, which characterizes the tailedness of the distribution and is associated with the impulsive hits generated by the faults. The most widely used algorithm for this purpose is the Fast Kurtogram (FK) [28], which has been proven effective in the case of cavitation detection in open [32], [33] and closed [22] hydraulic turbomachinery.

The differentiation between open and closed hydraulic turbomachinery is based on the type of flow in the machine, i.e. closed means that the flow is bounded from a casing (e.g. centrifugal pumps and reaction hydro-turbines), while open flow conditions are mainly exhibited in the case of propellers in marine applications. This differentiation is important because it influences the modulation frequency, based on which the cavitation detection is achieved. More specifically, the dominant flow excitation in closed machines is the pressure pulsations from the interaction between the rotor and the stator [1], [34]–[36]. The rotor-stator excitation results in the widely discussed BPF component that is aimed to be minimized during the design of hydraulic machines, while the poorer design results in stronger excitations. On the other hand, in open machines the flow is free from this interaction and the pressure field generated is less modulated from the rotating parts. For this reason, the SES results in the case of closed machines highlight the presence mainly of BPF component, while for open machines the shaft Rotation Frequency (RF) usually appears.

In the same direction of revealing the relation between the modulations and the carriers in signals of rotating components towards fault diagnosis, the use of spectral correlation estimation has been



proposed [37]–[41]. More specifically, the calculation of the Cyclic Spectral Correlation (CSCor) and its normalized by the signal power version, Cyclic Spectral Coherence (CSCoh) have been proved very effective on revealing the hidden periodicities of second-order cyclostationarity in signals [42], [43], where impulsive nature fault mechanisms are masked from the overall machine noise [44]–[46]. In the case of cavitation, the identification of the resonances [47]–[49] and the study of the shaft modulation amplitudes that are calculated after the integration of all the carries in both CSCor and CSCoh bi-variable maps [50] has been used as a tool for effectively characterizing the phenomenon.

The study of the literature concludes that the approaches, which identify the resonances and their modulations can be exploited towards cavitation diagnosis. The interaction of the vapor bubble implosions with the machine rotating flow field and structure hides useful diagnostic information, which has to be unveiled with the proper use of signal processing methods and the effective formation of diagnostic indicators. However, especially in the case of cavitation that is a failure mechanism hard to be studied, the literature results are usually incomplete, since the various approaches are applied in a very small number of operating conditions, most often not more than two (i.e. health vs cavitation) and it is not attempted to discuss and evaluate them against different suction pressure and load (i.e. flowrate) conditions as well as against different geometrical characteristics. Furthermore, the published works do not include an evaluation of the proposed methodologies against their ability to perform robust diagnosis of the two phase flow structures.

The present study targets to cover the aforementioned gaps by investigating the applicability of the HT- and CSCor-based envelope spectra to identify cavitation initiation and development in two impellers with different geometrical characteristics (number and angles of blades) that each of the two is operated in four flowrates, while for each flowrate an average of nine different Net Positive Suction Head (NPSH) conditions are tested. In addition, the current work proposes the use of Improved Envelope Spectrum (IES) for the cavitation diagnosis in closed hydraulic turbomachinery, where cavitation resonances can be found from the examination of CSCor, CSCoh and frequency spectrum results. Moreover, the formation of indicators based on the envelope spectra amplitudes of all possible combinations of characteristic frequency components is proposed and the latter are evaluated with the use of two criteria, (i) the efficient diagnosis of cavitation and (ii) the indicator robustness. The signal processing methodologies are applied on the raw data acquired from an accelerometer at the casing of the pump. It is also highlighted that the first evaluation criterion exploits the ground truth information provided from the direct visual measurements, acquired from both impellers' flow paths, regarding the phenomenon initiation.

The methodology proposed in this work is presented in Section 2, including the description of the experimental set up along with the presentation of the pumps' characteristic curves and the vibration and camera raw results (Section 2.1), the mathematical formulation of the signal processing approaches applied (Section 2.2) and the indicator formation strategy and evaluation (Section 2.3). Finally, Section 3 discusses the results with respect to (i) the FK, CSCor and CSCoh maps (Section 3.1), (ii) the envelope spectrum results and (iii) the behavior and performance of the diagnostic indicators (Section 3.3). The paper closes with some conclusions.

## 2. Methodology

The methodology of this work is analyzed in this section. As explained in the introduction, the aim of this work is the drawing of firm conclusions on the applicability of cyclic spectrum-based indicators towards the detection of cavitation in rotating flow fields, which exhibit different pressure, flowrate and geometric characteristics. In order to achieve this aim, different experimental, signal processing and analysis steps have to be implemented. The latter are described from the flow chart of Fig. 1. At first, an experimental set-up that incorporates a centrifugal pump is used to generate, with the use of two different impellers, the rotating flow fields under study. On the pump casing and close to the point of

the minimum pressure in the flow field, an accelerometer is installed that measures the dynamic vibration signal, while a camera acquires images that depict the flow path and identifies the existence of two-phase flow structures. For each operating condition of each impeller tested, the acquired signals are subjected in splitting into smaller windows segments, estimating signal's envelope spectrum and formatting of the cyclic spectrum-based indicators. From the processing of the images, the operating point, where the first vapor bubbles are visually observed is identified and consequently the thresholds are calculated based on the healthy data. The last step of the methodology is to evaluate the indicators, based on the number of missed detection and false alarms and based on their robustness. The Sections 2.1-2.3 provide the details of the experimental set-up, the cyclic spectrum estimation approaches and the health indicators formation and evaluation, respectively.

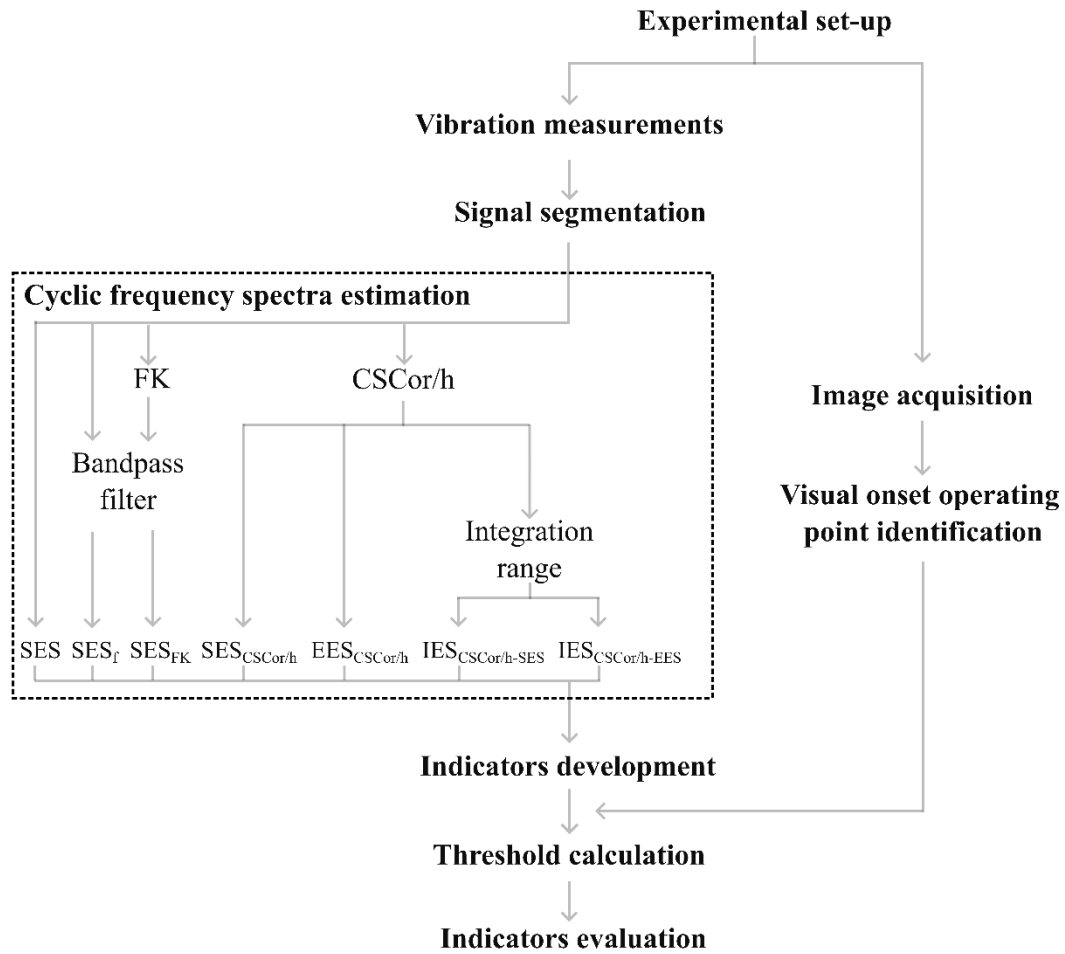


**Figure 1** Methodology flowchart.

## 2.1 Experimental set-up

The vibration signals are acquired from the experimental and data acquisition set-up of the Renewable Energy Group of Lancaster University [51], described also in [20], [22]. The test rig is an open sump with throttle valve type cavitation test rig (Fig. 2) made up by a centrifugal pump (Fig. 2, (1)), the tank (2) and the piping system, it is manufactured by Turbine Technologies Ltd and all parts are transparent in order to allow the user to visual observe the flow conditions (single or two-phase flow). The pump is coupled with a variable speed ABB induction motor (Fig. 2, (3)) of 2.3 kW rated power output at rated rotational speed,  $\Omega=1750$  rpm. The speed of the motor is controlled with the use of a potentiometer, while the amount of flowrate that enters the pump and the NPSH can be adjusted with the use of the manual suction (Fig. 2, (4)) and discharge (5) valves, respectively. The pump does not have bearings and the loads generated are transferred to the motor bearings (type: 6207 and 6203),

allowing the minimization of mechanical noise generated, while benefiting the identification of fluid related excitations. As discussed in [20], [22], five physical quantities are also measured along with the vibration signals, the static pressure measurements at the suction,  $p_e$  (Fig. 2, (i)), and the discharge,  $p_a$  (ii) of the pump, the flowrate (iii),  $Q$  at the discharge of the pump, the torque of the motor (iv),  $M$ , the rotational speed of the motor (v),  $\Omega$ , and the water temperature (vi),  $T$ . These measurements are referred in the text as low sampling frequency,  $f_s$ , quantities since they are acquired with  $f_s=1$  kHz.

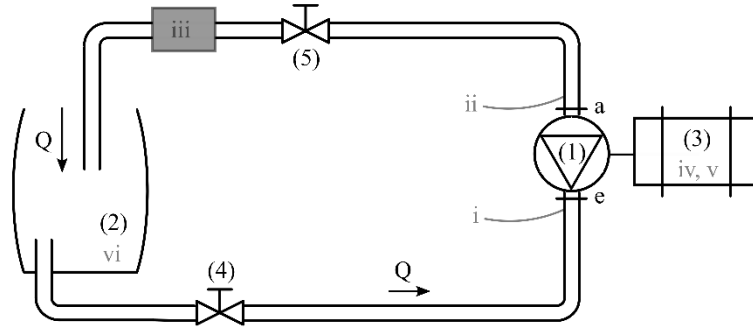


**Figure 2** Sketch of the cavitation experimental set-up.

In this study, the set-up is used in order to operate the pump under different cavitating conditions and to generate the vibration signals that are subsequently used for the evaluation of the health indicators. Moreover, this work aims to evaluate the different methodologies in a range of load conditions and geometrical characteristics. The latter is achieved by using the two semi-open impellers presented in [22], while for each impeller, 4 different load conditions are examined. The two impellers have the same inlet and outlet diameters, use the same nozzle and are installed in the same volute, while they have different blade angles and impeller No.1 uses 6 main and 6 splitter blades (all backward curved) and impeller No. 2 uses 12 main radial blades.

$$NPSH = \frac{p_e}{\rho g} + \frac{8Q^2}{g\pi^2 d_{p,e}^4} - \frac{p_{sat}}{\rho g} \quad (1)$$

$$p_{sat} = (0.1907T - 1.5157) \cdot 1000 \quad (2)$$

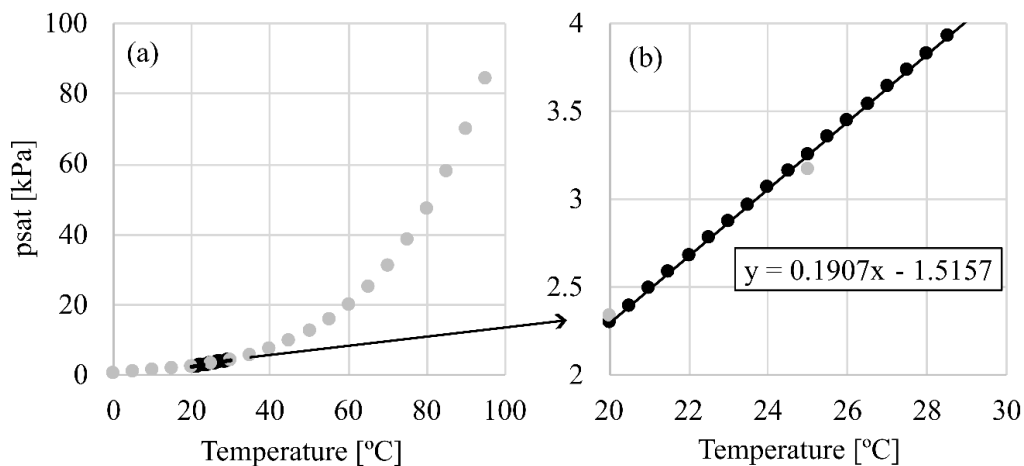


**Figure 3** (a) Water saturation vapor pressure as function of temperature, (b) the assumed linear range for [20-30] °C.

The NPSH value of the hydraulic configuration can be calculated from Eq.1, where  $\rho$  is the fluid density,  $g$  is the gravitational acceleration,  $d_{p,e}$  is the inner diameter of the of suction pipe and  $p_{sat}$  is the saturation pressure. The latter is a function of temperature of the working fluid, and for water it is approximated

by Eq. 2, derived from Fig. 3b, after assuming a linear relation between the temperature and the medium's saturation pressure for the range [20-30] °C. In this test, the fluid temperature remains in this range ensuring the proper use of Eq. 2.

In order to decrease the NPSH level of the hydraulic configuration, the suction valve is gradually closed resulting in an increase of the losses at the suction pipe that consequently influence NPSH as shown in Eq. 3. Here,  $H_E$  is the pressure at the surface of the tank expressed in meters,  $\Delta H_{z,e}$  is the height difference between the pump suction and the surface of the tank and the  $\zeta_e$  is the losses factor of the suction pipes. In the case of open tanks, as the one used in this study,  $H_E$  can be calculated from Eq. 4.

$$NPSH = H_E - \Delta H_{z,e} - \zeta_e Q^2 - H_{sat} \quad (3)$$

$$H_E = p_{atm}/\rho g \quad (4)$$

Moreover, in order to ensure that the flowrate remains constant during the NPSH decrease, the closing of the suction valve is followed by the opening of the valve at the pump discharge (a). This implies that at the beginning of the test the discharge valve should not be fully open, which limits the current set-up to test up to the best efficiency point (BEP) flowrate for each impeller. In Fig. 4 a graphical representation of the raw pressure, flowrate, torque and speed measurements trends is presented for a full test that corresponds to one flowrate. In this case, a cavitation test that includes ten different operating points (OP) is shown. Here, the progressive decrease of the pressure level in the hydraulic configuration is depicted in the  $p_e$  and  $p_a$  measurements, along with the constant speed and flowrate conditions applied during the full test. As show in Fig. 4, the acquisition time,  $t_s$  of the low  $f_s$  quantities is 2 minutes, while between two OPs, the valves opening are adjusted and an additional 30 sec waiting time is added in order to let the flow conditions to be stabilized.

$$H_{tot} = H_{oa} - H_{oe} = \underbrace{\frac{p_a - p_e}{\rho g}}_{\Delta H_{st}} + \underbrace{\frac{8Q^2}{\pi^2 g} \left( \frac{1}{d_{p,a}^4} - \frac{1}{d_{p,e}^4} \right)}_{\Delta H_{dyn}} + \underbrace{z_a}_{\Delta H_z} \quad (5)$$

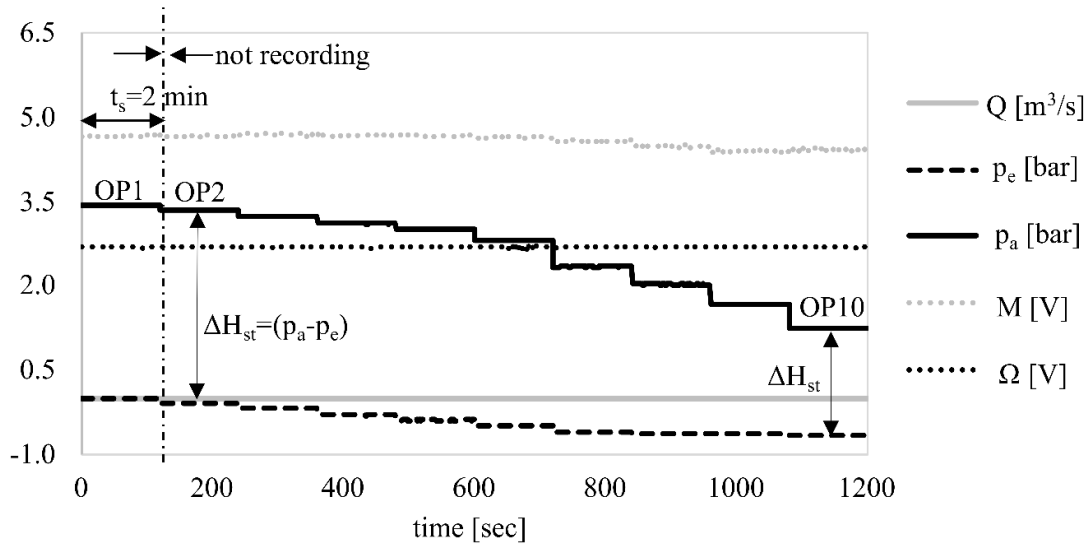


**Figure 4** Graphical representation of typical raw measurements of the pressure ( $p_e$ ,  $p_a$ ), flowrate ( $Q$ ), torque ( $M$ ) and speed ( $\Omega$ ) conditions during a cavitating condition test.

From the low  $f_s$  quantities, the total energy per unit weight transmitted from the rotating impeller to the fluid is calculated from the  $H_{tot}$  Eq. 5. Here,  $H_{oa}$  and  $H_{oe}$  are the total energy per unit weight at the discharge and the suction side of the pump, respectively,  $d_{p,a}$  is the inner diameter of the suction pipe and  $z_a$  indicates the vertical distance between the two static pressure installation points at the suction and the discharge of the pump. The energy difference is formed from three terms, (i)  $\Delta H_{st}$ , (ii)  $\Delta H_{dyn}$  and (iii)  $\Delta H_z$  that represent the static, dynamic and potential energy of the fluid, respectively.

In Fig. 4, it is also clear that the difference between  $p_a$  and  $p_e$  that expresses the  $\Delta H_{st}$  term, decreases heavily as we move closer to the end of the test (OP 10). This drop reflects the drop of total head of the machine at the minimum suction pressure conditions, as it is presented in Fig. 5. As expected, this drop is not related neither with the changes in the flowrate (which is kept constant) and the geometric characteristics of the hydraulic configuration, but purely with the static pressure and the development of the cavitating flow. A similar but less evident decreasing trend is also exhibited by the torque measurement, which reflects the load decrease due to the formation of the vapor areas in the impeller. In this work, the full test described in Fig. 4 is repeated for three times for each flowrate condition in order to check and ensure the repeatability of the measurements.

$$\Phi = \frac{2Q}{(\pi D_2 - z_s q_2) b_{1,2} \Omega D_2} \quad (6)$$

$$\Psi = 8gH_{tot}/(\Omega D_2)^2 \quad (7)$$

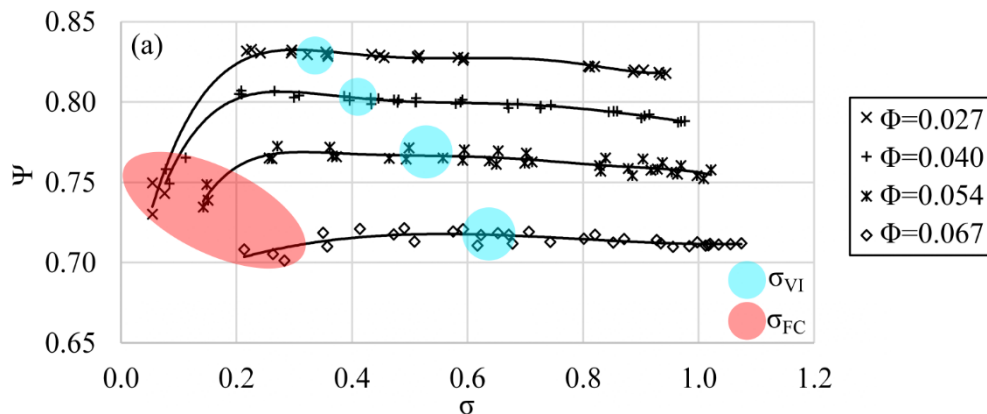
$$\sigma = NPSH/H_{tot} \quad (8)$$

The flowrate, the total head and the NPSH are non-dimensionalized based on the Eqs. 6-8, respectively. Here,  $D$  is the impeller diameter,  $z_s$  is the number of impeller blades,  $q$  is the blade thickness and  $b$  the blade width. In this work, the subscripts 1 and 2 symbolize the point at the inlet and the outlet of the blade, respectively. All the geometrical characteristics of the set-up that are used in Eqs. 1-8 are shown in Table 1.

**Table 1** Pump and impeller geometrical characteristics.

Impeller	$d_{p,e}$ [m]	$d_{p,a}$ [m]	$z_a$ [m]	$D_2$ [m]	$z_s$	$q_2$ [m]	$b_{1,2}$ [m]
No. 1	0.047	0.041	0.305	0.165	12	0.0101	3
No. 2						0.0059	3.1

The  $\sigma$ - $\Psi$  characteristic curves from both impellers are given in Fig. 5, accompanied by the points of (i) the visual observation of the first vapor bubble ( $\sigma_{VI}$ ) and (ii) the fully cavitating condition ( $\sigma_{FC}$ ) at the minimum  $\sigma$ . The plots include the points derived from the three repeatable tests for each flowrate. The largest flowrate of impeller No. 1 equals the BEP flowrate ( $\Phi_{BEP}$ ) at the point of maximum efficiency, while in the case of impeller No.2 equals to  $0.96 \Phi_{BEP}$ . The lower the  $\Phi$  value tested, the higher is the  $\Psi$  value calculated and as the  $\sigma$  decreases, the onset of cavitation is visually observed at  $\sigma_{VI}$  and the drop of the head at  $\sigma_{FC}$ .



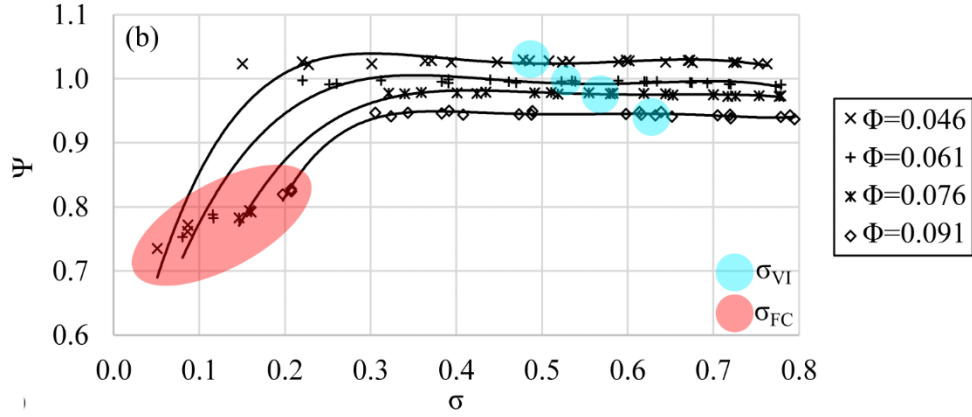


**Figure 5** Cavitation  $\sigma$ - $\Psi$  characteristic curves for impeller (a) No.1 and (b) No.2.

During the 2 minutes acquisition of the low  $f_s$  results (Fig. 4), the images that depict the macroscopic quasi-steady state type of flow are also acquired with the use of a camera. In this way it is possible to confirm the presence and the extent of the vapor phase inside the impeller's flow field. As it is discussed in section 2.3, the current work exploits the camera information and more specifically the point of the visual inception in order to evaluate the indicator developed in section 2.3. In Fig. 6, one image from the visual onset and one from the fully cavitating OPs are shown for one flowrate of each impeller. The images confirm the presence of cavitation bubbles and the increase of their extent with the decrease of  $\sigma$  value.

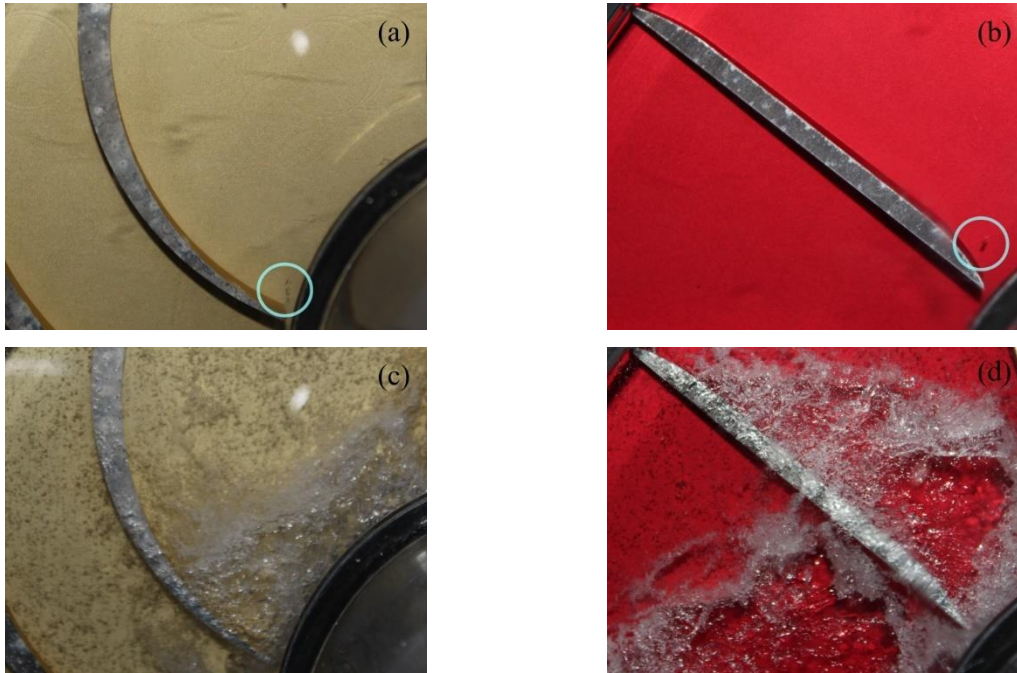


**Figure 6** Visual inception OP at impeller No.1,  $\Phi=0.040$ ,  $\sigma_{VI}=0.39$  (a),  $\sigma_{FC}=0.08$  (c), and impeller No.2,  $\Phi=0.061$ ,  $\sigma_{VI}=0.52$  (b),  $\sigma_{FC}=0.12$  (d).

In parallel with the camera acquisition, the vibration signal is acquired with the accelerometer B01 [22] at  $f_s=20$  kHz for a duration of 30 seconds. The accelerometer is positioned on the casing of the pump close to the area of the visual onset of the phenomenon and is used in order to acquire the signals that are processed with the methods discussed in section 2.2. Moreover, the signals are further processed so as to derive indicators that are evaluated based on their effectiveness to detect cavitation in a wide range of operating conditions ( $\sigma$  &  $\Phi$ ) of the two impellers. In several studies [16], [17], [22], [25], [32], [33],

[47], [49], [50], [52]–[54], it has been proven that the initiation of a stochastic and of impulsive nature phenomenon, such as cavitation, inside a rotating flow field, such as the one of hydraulic turbomachinery (centrifugal pumps, reaction hydro-turbines, propellers etc.) that is highly modulated by the shaft and the blade passing frequencies, can excite resonances that may act as a carrier of the aforementioned modulations. The more extreme the cavitating conditions, the clearer is the existence of random nature impulses that form amplitude modulated peaks in the vibration signal acquired from hydraulic turbomachines. This behavior can be also confirmed in the raw vibration time-series acquired from impeller No. 2 and is presented in Fig. 7.

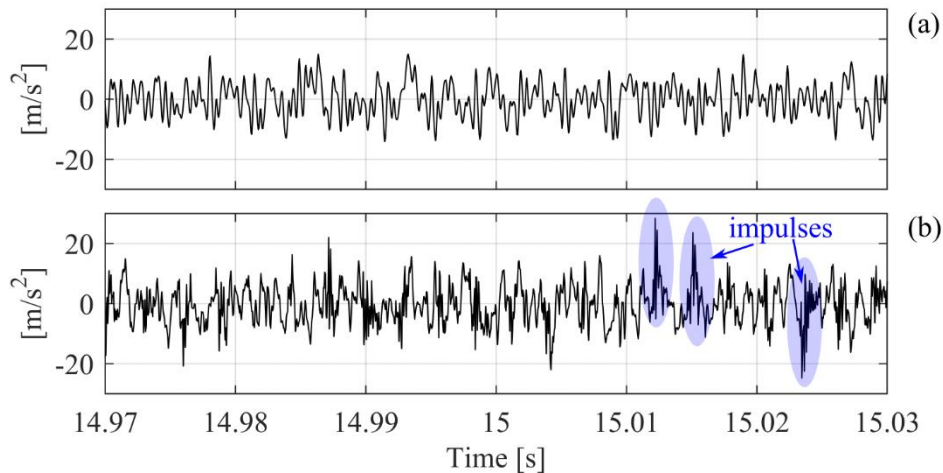


**Figure 7** Raw vibration time series for impeller No. 2,  $\Phi=0.061$  at (a)  $\sigma_{VI}$  and (b)  $\sigma_{FC}$ .

For the processing of the vibration signals it is important to know the values of the characteristic frequencies that are generated from the machine components. In a centrifugal pump, such as the one used in the case of this study, the main component is the shaft RF and its harmonics, including the BPF. In this experiment, RF is constant and equal to 30 Hz, impeller No. 1 has 6 main blades (i.e. BPF=180 Hz) and 6 splitter blades that give a total blade passing frequency (TBPF) equal to 360 Hz, while impeller No. 2 has 12 straight blades that results in a BPF equal to 360 Hz. Finally, after the 30 seconds duration vibration signals are acquired, they are segmented in 15 parts of 2 seconds in order to allow the evaluation of the different indicators with the robustness criterion presented in section 2.3. The waiting time of 30 sec after the regulation of the discharge valve ensures that the vibration signals correspond to pump steady state conditions and the information acquired is uniformly spread in them. For this reason, the segmented signals do not overlap. The signal segmentation reduces the resolution of the Fast Fourier Transform and the cyclic frequency spectrum of CSCor map respectively from 0.033 to 0.5 Hz, i.e. remaining in an acceptable resolution value that is able to recognize the expected aforementioned excitations and modulations. Moreover, the longer periodicity expected to be measured is the shaft rotation that is 20 times smaller than the segmented signal duration (2 seconds). The reduction of the resolution value will also not affect the carriers estimation, since those are expected to cover a wide range of frequencies as has been shown in past cavitation studies [22], [47], [50], [55].

## 2.2 Estimation of the Envelope Spectrum

The signals used in this work are processed with eleven ways that all aim to give an estimation on the envelope spectrum (ES). In addition, these approaches are grouped with respect to two criteria; the first one is the main modulation estimation approach, while the second is the degree of intervention required by the user. More specifically, from the first criterion, the envelope spectra can be either the result of the HT or the CSCor methodology. From the second criterion, there are envelope spectra estimated without any intervention by the user, while other need some additional guidance that focuses on the frequency bandwidth of the expected carriers excited from the phenomenon. Before the presentation of

the equations of the various methodologies, the latter are split in different categories and presented in Table 2.

**Table 2** Overview of the Signal Processing approaches used for the envelope spectrum estimation.

<b>Carrier bandwidth unknown</b>		<b>Abbreviation</b>
1	*Squared Envelope Spectrum (SES)	SES
2	**Filtered Squared Envelope Spectrum after using the Fast Kurtogram	SES <sub>FK</sub>
3	**Squared Envelope Spectrum based on CSCor	SES <sub>CSCor</sub>
4	**Enhanced Envelope Spectrum (EES) based on CSCor	EES <sub>CSCor</sub>
5	**Squared Envelope Spectrum based on Cyclic Spectral Coherence (CSCoh)	SES <sub>CSCoh</sub>
6	**Enhanced Envelope Spectrum based on CSCoh	EES <sub>CSCoh</sub>
<b>Carrier bandwidth provided</b>		
7	*Filtered Squared Envelope Spectrum	SES <sub>f</sub>
8	**Improved Envelope Spectrum (IES) based on CSCor SES	IES <sub>CSCor-SES</sub>
9	**Improved Envelope Spectrum based based on CSCor EES	IES <sub>CSCor-EES</sub>
10	**Improved Envelope Spectrum based based on CSCoh SES	IES <sub>CSCoh-SES</sub>
11	**Improved Envelope Spectrum based based on CSCoh EES	IES <sub>CSCoh-EES</sub>

\*Hilbert Transform-based ES / \*\*Cyclic Spectral Correlation-based ES

### The Hilbert Transform-based Squared Envelope Spectra

The SES results from the algorithmic execution of three different steps; (i) the calculation of the signal's envelope,  $e_d(n)$ , through the Hilbert Transform, (ii) the squaring of the envelope in the time domain, and (iii) the calculation of the frequency spectrum of the latter. The estimation procedure for the first step is mathematically described from Eqs. 9-11 [23]. At first, the Fast Fourier Transform (FFT)  $X(k)$  of the discretized signal,  $x(n)$ , is estimated by Eq. 9:

$$X(k) = \frac{1}{N} \sum_{n=0}^{N-1} x(n) e^{-\frac{j2\pi kn}{N}}, k = 0, \dots, N-1 \quad (9)$$

where,  $N$  is the sample length. The Hadamard product  $Z(m)$ , of  $X(k)$  with  $H(m)$  is then calculated by Eq. 10:

$$Z(m) = H(m) \odot X(k), \quad \text{where } H(m) = \begin{cases} 1, & \text{for } m = 1, \left(\frac{N}{2}\right) + 1 \\ 2, & \text{for } m = 2, 3, \dots, \left(\frac{N}{2}\right) \\ 0, & \text{for } m = \left(\frac{N}{2}\right) + 2, \dots, N \end{cases} \quad (10)$$

Next, the analytic signal  $A_s(n)$  can be calculated by the implementation of the  $N$ -point Inverse FFT of  $Z(m)$  as shown in Eq. 11:

$$e_d(n) = |A_s(n)| = \left| \sum_{m=1}^N Z(m) e^{\frac{j2\pi mn}{N}} \right| \quad (11)$$

The magnitude of the  $A_s(n)$  is the discrete signal's envelope,  $e_d(n)$ . The latter, is then squared and the SES is calculated from Eq. 12:

$$SES(k) = \left| \frac{1}{N} \sum_{n=0}^{N-1} e_d(n)^2 e^{-\frac{j2\pi kn}{N}} \right|, k = 0, \dots, N-1 \quad (12)$$

The filtered SES ( $SES_f$ ) and the Fast Kurtogram-based SES ( $SES_{FK}$ ) are estimated from the same procedure described from Eqs. 9-12, with the only exception that the raw digitized signal  $x(n)$  is firstly passed from a digital bandpass filter. In the case of  $SES_f$ , the filter central frequency,  $f_c$  and bandwidth,



bw are selected from the authors ( $f_c=8$  kHz,  $bw=4$  kHz), based on the frequency spectra and FK results of previous works on the same machine ([20], [22]) that highlighted the excitation of the high frequency ranges from the bubble implosions that exhibit non-stationary behavior. The filter used for the  $SES_f$  estimation remains the same for all conditions discussed in this work. On the other hand, the FK-based SES ( $SES_{FK}$ ) uses the filter outputted from the FK filter-bank algorithm [28] that exhibits the maximum kurtosis value. To accomplish this calculation, the FK maps the kurtosis values across various frequency bands using Eq. (13):

$$K(f) = \frac{\langle |X(t, f)|^4 \rangle}{\langle |X(t, f)|^2 \rangle^2} - 2 \quad (13)$$

where  $|X(t, f)|$  is the filtered signal complex envelope around a frequency  $f$ . In this case, the filter characteristics resulted, can change when different operating conditions are tested [22].

#### *The Cyclic Spectral Correlation and Coherence-based envelope spectra*

An alternative ES estimation can be achieved with the use of the Spectral Correlation that has been proposed from the identification and characterization of cyclostationary signals [37], [38] and is calculated from Eq. 14:

$$CSCor_x(\alpha, f) = \lim_{T \rightarrow \infty} \frac{1}{T} \mathbb{E}\{F_T[x(t)]F_T[x(t + \tau)]^*\} \quad (14)$$

where  $F_T[x(t)]$  is the Fourier transform of the signal  $x(t)$  over the time period  $T$ ,  $\tau$  is the time lag and  $*$  is the complex conjugate. The Eq. 14 results in a bi-variable map made by the spectral ( $f$ ) and cyclic ( $\alpha$ ) frequency components that characterize the carrier and the modulating signals, respectively. For cavitation, it is expected that the resonances excited from the impulsive fault mechanism act as the carriers modulated from the dominant flow excitations, i.e. the shaft, the blade passing frequencies and their harmonics. The calculation of CSCor is done with the Fast Spectral Correlation algorithm [42], [43] that can reveal the correlation between the frequency and the cyclic frequency values, i.e. between the carriers and the modulations in the measured signal. Moreover, this work aims to examine and compare also the use of the Cyclic Spectral Coherence (CSCoh), which is the non-dimensional version of the CSCor, normalized by the signal power:

$$CSCoh_x(\alpha, f) = \frac{CSCor_x(\alpha, f)}{\sqrt{CSCor_x(0, f) CSCor_x(0, f - \alpha)}} \quad (15)$$

Last but not least, from the bi-variable CSCor and CSCoh maps, it is possible to calculate the Squared, the Enhanced and the Improved Envelope Spectra (IES) introduced in Table 2, from Eqs. 16-19. For the IES, the equations used are the same with those for CSCor- and CSCoh-based Squared and Enhanced Envelope Spectra and it is only differentiated with respect to the frequency integration range that in this case is the same frequency band ( $[f_1, f_2]=[6, 10]$  kHz) proposed by the authors for the  $SES_f$  is used. On the other hand, the Squared and Enhanced Envelope Spectra are calculated based on the full frequency range determined from Nyquist frequency, i.e.  $[f_1, f_2]=[0, 10]$  kHz.

$$SES_{CSCor}(\alpha) = \left| \int_{f_1}^{f_2} CSCor(\alpha, f) df \right| \quad (16)$$

$$EES_{CSCor}(\alpha) = \int_{f_1}^{f_2} |CSCor(\alpha, f)| df \quad (17)$$

$$SES_{CSCoh}(\alpha) = \left| \int_{f_1}^{f_2} CSCoh(\alpha, f) df \right| \quad (18)$$

$$EES_{CSCoh}(\alpha) = \int_{f_1}^{f_2} |CSCoh(\alpha, f)| df \quad (19)$$

### 2.3 Health Indicators formation and evaluation

The envelope spectra estimated with the methods described in section 2.2, reveal the modulations on the signal measured from the experimental set-up. In the case of closed hydraulic turbo-machinery, the vibration signals are dominated and modulated from the pressure pulsations caused from the rotor (impeller/runner) interaction with the non-axisymmetric flow and geometry of the casing (volute). The latter is generated from the unevenly distributed flow at the spiral casing and the effect of the volute tongue. More specifically, in centrifugal pumps it is the result of the pitch-wise non-uniform velocity profile at the outlet of the impeller, while in reaction hydro-turbines at the inlet of the runner [1], [34], [35]. Thus, the rotor-stator interaction produces a flow field which is dynamic and is dominated from the shaft rotational (RF) and the blade passing frequencies (and their harmonics) [56]. This behavior characterizes the machines when operate under non-cavitating conditions and it becomes stronger the further away from the BEP the hydraulic turbomachinery operates [57].

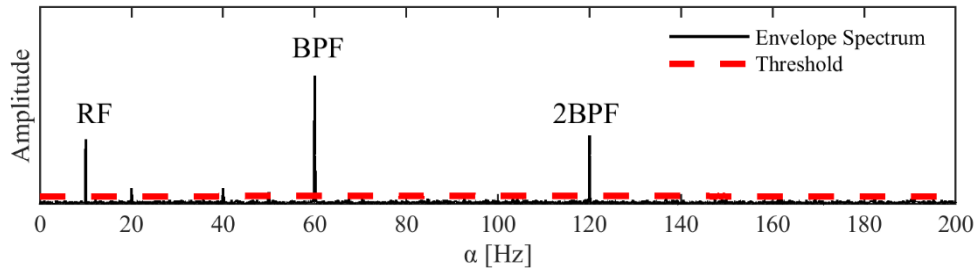


**Figure 8** Qualitative representation of the cyclic modulations of a closed hydraulic machine that uses 6 blades and rotates at 600 rpm.

The flow field modulations are transmitted in the mechanical structure of the machine and dominate its vibrations response measured with the accelerometers. For this reason, the frequency and the envelope spectra of a closed hydraulic turbomachinery that operates under non-cavitating conditions consists of peaks at RF and BPF cyclic frequency components that characterize the rotor-stator interaction, as presented in the sketch of Fig. 8. Moreover, the vapor bubble implosions during the onset and development of cavitation in the flow has been also proven to be modulated from the aforementioned dominant components of rotating machinery (RF & BPF) [16], [22], [25], [54]. Consequently, when the aim is to diagnose cavitation in a closed hydraulic turbomachinery with the use of the ES results, it is often hard to differentiate since the RF and BPF peaks appear in both healthy and cavitation spectra. In addition, the definition of a threshold at the level of the ES could complicate the cavitation diagnosis, because, as it is shown in Fig. 8, the RF and BPF peaks are clearly outliers that lead in false alarms in the case of cavitation. This behavior is also noticed in the case of gear monitoring, where the shaft modulations are observed under the healthy operation of gears [58], [59].

In order to avoid the aforementioned confusion and ensure a proper comparison of the various demodulation methodologies, the thresholds are applied at the level of the indicator. More specifically, the indicators are calculated based on the amplitudes of the main modulations expected to be observed in the ES results (Tables 3, 4). For the case of closed hydraulic turbomachinery those are the RF, BPF, 2BPF and the RF sidebands of the BPF. Such sidebands have been observed in SES of heavy cavitating condition [22] and imply a second modulation of the shaft to the main BPF modulation. For this reason they are also investigated in this study. Impeller No.1 has 6 main blades and 6 splitter blades, thus the TBPF and its RF sidebands are also calculated increasing the number of indicators compare to impeller No.2. All combinations of discrete amplitudes for both impellers is shown in Tables 3 & 4. In addition, the image results and the characteristic curves of Fig. 5 reliably provide the information about the

signals that correspond to healthy cavitating conditions towards forming the threshold of each indicator for each flowrate and impeller tested. The latter calculation excludes the first point before the  $\sigma_{VI}$  (see Fig. 9), because at such conditions it is possible that the phenomenon has already initiated but the camera is not able to capture it due to the very rapid bubble creation and collapse. In this work, the Median Absolute Deviation (MAD) [60] (Eq. 20) is used for the threshold calculation (Eq. 21) of all the indicators:

$$MAD = 1.4826 \cdot M(|I - M(I_s)|) \quad (20)$$

$$t_{MAD} = 3 \cdot MAD \quad (21)$$

where,  $M$  is the median,  $I_s$  is the sample formed from all indicators that correspond to healthy conditions and  $I$  is the indicator value.

**Table 3** Indicators formed based on the amplitude and the sum of amplitudes of discrete cyclic components in impeller No.1.

Amp. No.	1	2	3	4	5	6	7	8	9	10	11	12	13	14	15	16	17	18	19	20
RF	x						x	x	x	x	x									
BPF		x					x					x	x	x	x					
TBPF			x					x				x				x	x	x		
2TBPF				x					x				x						x	x
BPF±RF					x					x				x			x			x
TBPF±RF						x					x				x			x		x
Amp. No.	21	22	23	24	25	26	27	28	29	30	31	32	33	34	35	36	37	38	39	40
RF		x	x	x	x	x	x	x	x	x	x									
BPF		x	x	x	x							x	x	x	x	x	x			
TBPF		x				x	x	x				x	x	x				x	x	x
2TBPF			x			x			x	x		x			x	x		x	x	
BPF±RF	x			x			x		x	x		x			x		x	x		x
TBPF±RF	x				x			x		x	x			x		x	x		x	x
Amp. No.	41	42	43	44	45	46	47	48	49	50	51	52	53	54	55	56	57	58	59	60
RF		x	x	x	x	x	x	x	x					x	x	x	x	x	x	x
BPF		x	x	x	x	x				x	x	x		x	x		x	x	x	x
TBPF		x	x	x			x	x		x	x		x	x	x	x		x	x	x
2TBPF	x	x			x	x	x	x	x	x	x	x	x	x	x	x			x	x
BPF±RF	x			x			x			x	x		x	x	x		x	x	x	x
TBPF±RF	x			x			x	x		x	x		x	x	x		x	x	x	x

**Table 4** Indicators formed based on the amplitude and the sum of amplitudes of discrete cyclic components in impeller No.2.

Amp. No.	1	2	3	4	5	6	7	8	9	10	11	12	13	14	15
RF	x					x	x	x			x	x	x		x
BPF		x				x			x	x		x	x		x
2BPF			x				x		x	x		x	x		x
BPF±RF				x				x		x		x	x		x

The indicators are evaluated based on two criteria. The first is the number of missed detections and false alarms that the use of the indicator resulted based on the MAD threshold set (Fig. 9). This criterion forms the Evaluation Score 1 (ES1) that is calculated based on Eq. 22, where  $N_{(I \leq MAD)_h}$  counts the number of times that, under healthy conditions, the indicator value,  $I$ , is lower than the MAD,  $N_{(I \leq MAD)_c}$  counts the number of times that, under cavitating conditions, the indicator value,  $I$ , is larger than the MAD and  $N_I$  corresponds to the number of indicator values used for the numerator calculation. In order to allow a proper comparison between all the indicators examined in this study, ES1 is normalized with the  $N_I$  value. In the case of a test where all fault conditions and only those ones are detected,  $ES1=1$ .

$$ES1 = \frac{N_{(I \leq MAD)_h} + N_{(I > MAD)_c}}{N_I - 1} \quad (22)$$

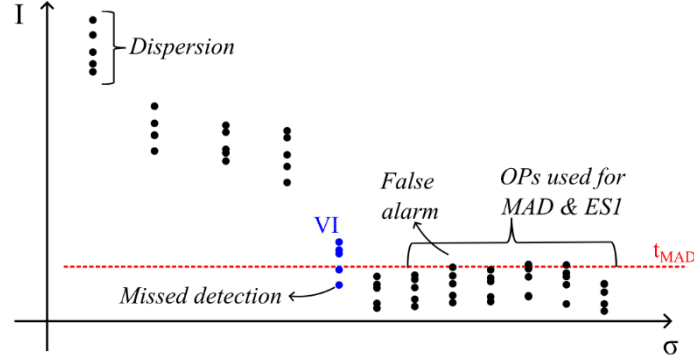


**Figure 9** Qualitative representation of the indicator trend at different suction pressure conditions.

The second evaluation criterion that forms ES2, is based on the dispersion of the indicator value (Fig. 9) calculated for one operating condition from the 15 segmented signals. The smaller variation exhibited from an indicator the more reliable it can be for cavitation diagnosis purposes. For comparison purposes the coefficient of variation,  $c_v$  is used in order to allow the non-dimensional representation of dispersion after normalizing the standard deviation of the 15 values with their mean, as show in Eq. 23. For a complete test of one flowrate  $Q$ , the mean of  $c_v$  gives an average measure of the indicator dispersion. The ES2 is then formed based on the maximum inverse mean  $c_v$  for each test performed, according to Eq. 24. Thus, in the case of ES2, for each flowrate tested, only one indicator exhibits ES2=1.

$$c_v = st. dev (I_{15}) / mean (I_{15}) \quad (23)$$

$$ES2 = \frac{1}{mean(c_v)_Q \cdot \max\left(\frac{1}{mean(c_v)_Q}\right)} \quad (24)$$

### 3. Results

The results from the processing of the pump vibration signals are presented in this section. At first the CSCor, CSCoh and FK maps are shown, followed from the different ES calculated under various NPSH and load operating points. In addition, the results of the cyclic spectra based indicators are given as a function of suction pressure conditions and are evaluated based on their ability to detect the phenomenon and their robustness.

#### 3.1 Cyclic Spectral Correlation/Coherence and Fast Kurtogram maps

Before presenting the ES results, the maps of CSCor, CSCoh and FK under healthy and cavitating conditions are shown in order to highlight the differences introduced by the development of the two phase flow formations and consequently influence the calculation of the SES, EES and IES. The maps are plotted in Figs. 10 and 12 for the impeller No.2 operating at  $\Phi=0.046$  under healthy ( $\sigma_H=0.75$ ) and fully cavitating conditions ( $\sigma_{FC}=0.09$ ). The selection of the impeller and flowrate is made in order to start the analysis with the geometry and the load conditions that exhibit the biggest incidence angle and relative flow velocity at the leading edge of the blade and result in highest noise and vibration [20]. Both CSCor and CSCoh values are estimated up to 1 kHz cyclic frequency, i.e. they include the modulations up to the second BPF harmonic. Also, the FK is calculated up to the 5<sup>th</sup> k level, which results in a minimum bandwidth of 312.5 Hz for the filters investigated in this study.

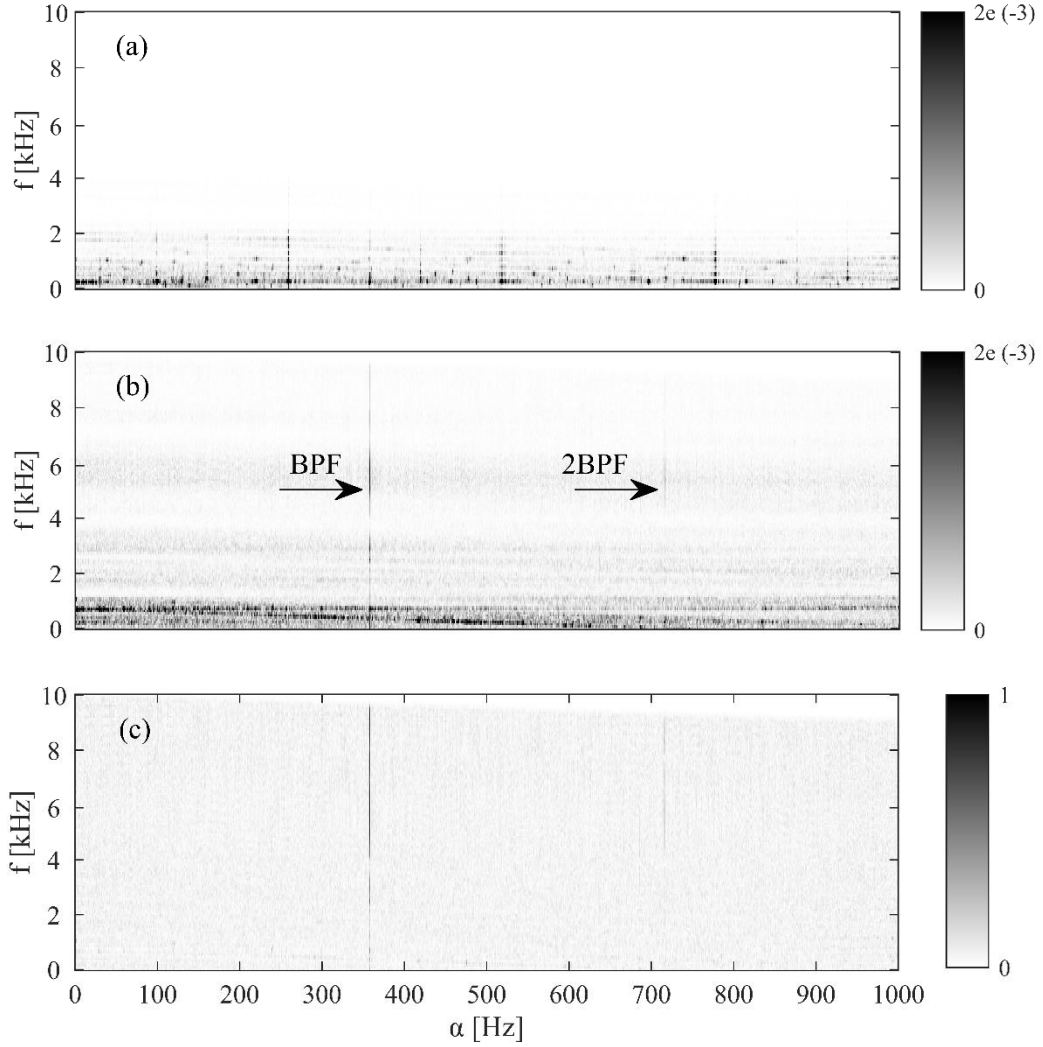


**Figure 10** (a) CSCor,  $\sigma_H = 0.75$ , (b) CSCor,  $\sigma_{FC} = 0.09$ , and (c) CSCoh,  $\sigma_{FC} = 0.09$  for impeller No.2,  $\Phi=0.046$ .

Under healthy conditions, CSCor exhibits low values for all high ( $>2$  kHz) frequency carriers no matter the cyclic component examined. On the other hand, under cavitating conditions, the correlation increases (i) for  $\alpha=BPF$  and  $f=[2-3] \cup [4-9]$  kHz, and (ii) for  $\alpha=2BPF$  and  $f=[4-7]$  kHz. For lower carriers in both healthy and cavitating conditions, the CSCor value exhibits also high values, however those are related with the signal energy since their value decreases to zero after the CSCor normalization with the power spectral density and the CSCoh calculation (Fig. 10c). For carriers with  $f>2$  kHz at  $\alpha=BPF$ , CSCoh exhibits similarly to CSCor maximum values that sometimes are even higher than 0.8. For both maps, under cavitating conditions the correlation and coherence values are stronger for the BPF cyclic component.

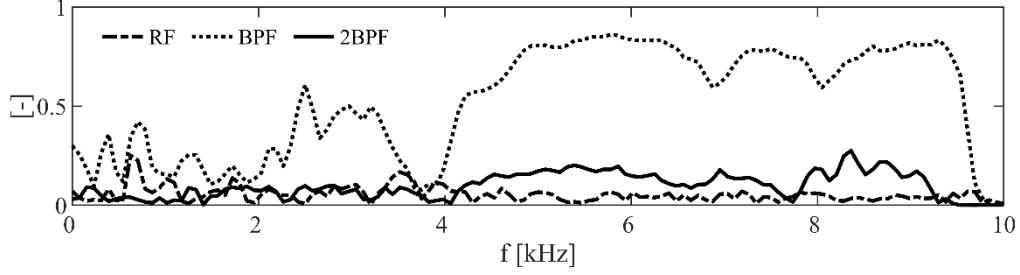


**Figure 11** CSCoh( $f$ ) for  $\alpha$ =RF, BPF, 2BPF for cavitating conditions of impeller No.2,  $\Phi$ =0.046.

The latter is also highlighted in the plot of Fig. 11, where the CSCoh is plotted only as a function of frequencies for three different cyclic components,  $\alpha$ =RF, BPF, 2BPF. Here, the increase of the coherence values for the aforementioned pairs of carriers and cyclic components, and especially for the BPF modulation, is also confirmed. The low frequency (<1 kHz) CSCoh peaks reveal the correlation of the cyclic components with the main hydro-mechanical excitations of the pump (i.e. the RF and BPF harmonics), while the wide peaks result from the frequency resolution ( $\sim 78$  Hz) as a consequence from the window size ( $2^8$ ) used in the STFT calculation of the CSCoh estimation. For the 2BPF the coherence amplitude is less strong but still reveals the carriers presented in Fig. 10 under cavitating conditions, while the RF in this case seems to be less correlated with the resonances excited from the phenomenon.

The findings of Fig. 11 are interesting because they also confirm the theoretical and experimental conclusions of various cavitation related published works. More specifically the BPF carriers shape is very similar with the schematic illustration presented by Wu ([49], [50]) for the second-order cyclostationary part of a simulated cavitation signal. The present work slightly differentiates on the cyclic component (BPF in Figs. 10 and 11) that mostly modulates the carriers similar to [16], [22], [25], [30], while in other experimental works the RF component seems to play a more critical role ([32], [48]–[50]). The dominant modulation highlighted in each work is dependent on the rotating flow boundaries and more specifically on the machine type (open or closed turbomachine) and the rotor and volute design quality. In order to delve deeper on this observation, the indicators formed and discussed in this article explore the contribution of the amplitude of discrete or sums of cyclic components towards the prompt and robust cavitation detection.

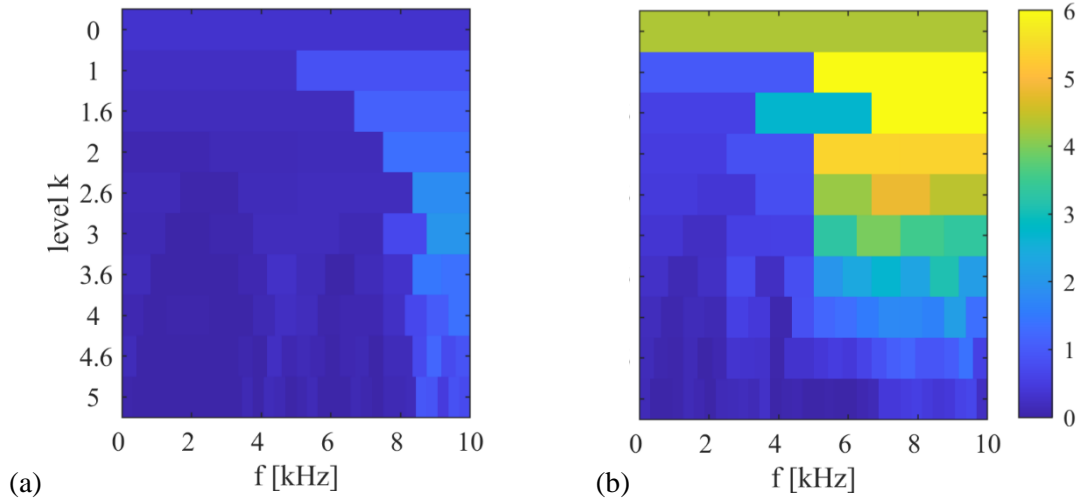


**Figure 12** FK at (a)  $\sigma_H = 0.75$  and (b)  $\sigma_{FC} = 0.09$  for impeller No.2,  $\Phi$ =0.046.

In addition to the correlation and coherence maps, in this section, the FK result is presented in Fig. 12 for the same operating conditions and the signal used in Fig. 11. As discussed in previous works [22], [32], FK can identify the frequency ranges excited from impulsive non-stationary nature sources, such as cavitation, and give rise on the kurtosis values of various bandwidths. This is also clear from the

comparison of the two maps of Fig. 12, where kurtosis value remains relatively low under healthy conditions but increases significantly for particular wide high frequency bandwidths. Moreover, it can be observed that the bandwidths with the highest kurtosis values in the cavitation case ([6.7-10] and [5-10] kHz) closely correlate with the ranges of the BPF carriers presented in Figs. 10 and 11 that exhibit the highest CSCor and CSCoh values. However, unlike CSCor and CSCoh maps, FK does not provide the information of the modulating components on those resonances. In order to do so, the Hilbert Transform has to be applied on the signal after the filtering of the later with the band pass filter resulted from the FK, as explained to section 2.2.

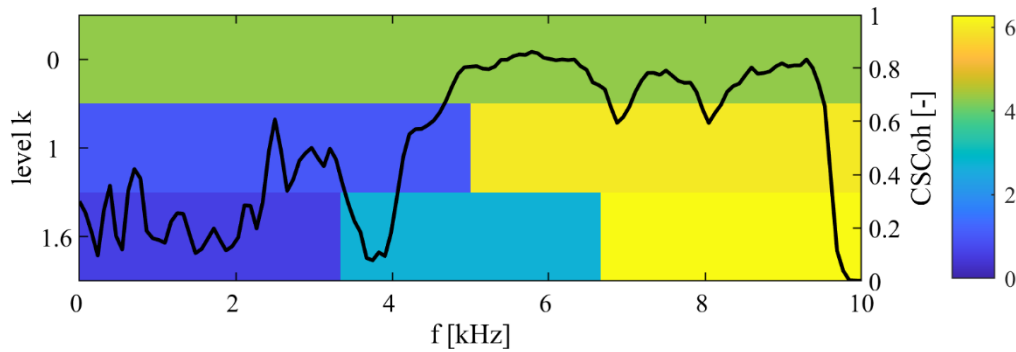


**Figure 13** CSCoh for  $\alpha$ =BPF on zoomed in FK map for impeller No.2 at  $\Phi=0.046$  and  $\sigma_{FC}=0.09$ .

In order to delve into the observation, the CSCoh for the dominant modulation ( $\alpha$ =BPF) is plotted on the zoomed in (level  $k=[0-1.6]$ ) FK map in Fig. 13. Here, it is concluded that both methodologies converge in similar frequency ranges, when it comes to the identification of non-stationarities. This conclusion is further discussed when the ES are calculated after filtering the raw data with the band pass filter of the FK. Another observation from Figs. 12 and 13 is that for  $\sigma_{FC}=0.09$  and even when level  $k$  value is equal to zero, a relatively high kurtosis value is calculated. This practically means that under heavy cavitating conditions the modulations on the impulsive cavitation waves are strong and can be revealed by the ES without using the filter proposed from the FK. This is further confirmed by plotting the raw signal in time in Fig. 14, where the impulses modulation at the blade passing period (1/BPF) and at the half of it (i.e. the 2BPF) can be observed. This case is also examined in the next section, where the results of the implementation of the HT on the raw signals are presented.

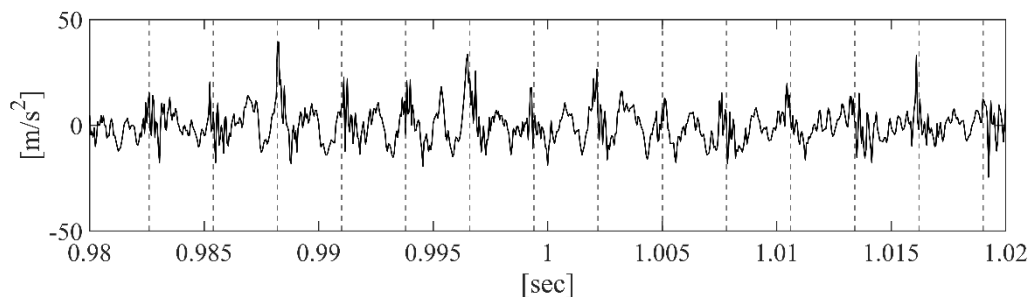


**Figure 14** Raw vibration signal for impeller No.2 at  $\Phi=0.046$  and  $\sigma_{FC}=0.09$ . The vertical dotted lines highlight the passing of each blade and their distance corresponds to 1/BPF.

### 3.2 Envelope Spectrum Analysis

As discussed in Section 2.2, eleven different cyclic spectra are calculated for each of the  $\sim 3000$  signals processed in this study. The analysis starts with the presentation of the cyclic spectra that correspond to the impeller and the operating conditions described in Section 3.1 (impeller No.2,  $\Phi=0.046$ ,  $\sigma_H=0.75$  and  $\sigma_{FC}=0.09$ ) and subsequently the influence of the geometry of the impeller along with the examination of the different flowrate ( $\Phi$ ) and suction pressure conditions ( $\sigma$ ) is investigated and discussed.

### Healthy vs fully cavitating conditions

The first two squared envelope spectra shown in Fig. 15 are those calculated with the use of the HT with ( $SES_{FK}$ ) and without (SES) the use of the filter provided from the FK. All cyclic spectra resulted from Spectral Kurtosis methodology are also accompanied from the central frequency  $f_c$  and the bandwidth  $bw$  of the filter implemented before the demodulation. Moreover all cyclic spectra presented in this section share the same x axis limits with maximum cyclic frequency,  $\alpha=1$  kHz. As it is shown, the two plots do not differ a lot, since both depict the clear modulation of the raw (SES) and the filtered vibration signal ( $SES_{FK}$ ) from the BPF and its second harmonic, when the pump operates under fully cavitating conditions. This result confirms the comment made for level  $k=0$  in the previous section. Also, it should be noted that the lower modulation amplitude for  $SES_{FK}$  ( $\sim 7$  (m/s<sup>2</sup>)<sup>2</sup>) compare to the SES ( $\sim 2$  (m/s<sup>2</sup>)<sup>2</sup>) results from the use of the position of the carrier with respect to the center of the filter. However it should be noted that for lower suction pressure conditions, where the phenomenon is less evident and the impulses are hidden from the hydrodynamic noise of the machine, the band pass filtering of the signal is expected to help towards revealing these modulations. Also, the amplitude of the 2<sup>nd</sup> BPF harmonic modulations exhibit larger or equal value compared to the first harmonic contrary to the results of Figs. 10 and 11, where BPF had higher correlation and coherence values. Under healthy conditions, the amplitudes calculated in both cases exhibit values are three orders of magnitude lower than the  $\sigma_{FC}$  and are barely noticeable in the plots.

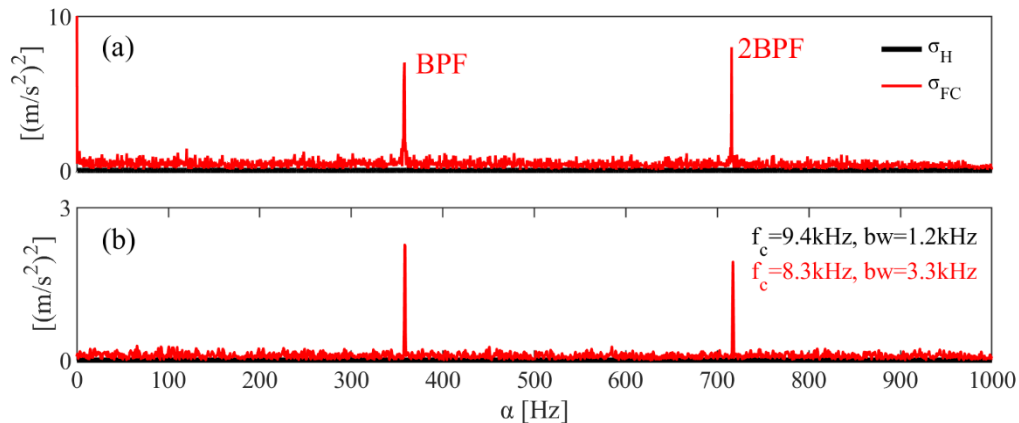


**Figure 15** (a) SES and (b)  $SES_{FK}$  for impeller No.2 at  $\Phi=0.046$  at healthy and cavitating conditions.

The next three spectra are given in Fig. 16 and correspond to  $SES_{CSCor}$ ,  $SES_{CSCoh}$  and  $EES_{CSCoh}$ , calculated from Eqs. 16, 18 and 19, respectively. As expected from the results of Fig. 10, the integration of the cyclic correlation and coherence values over the total carrier range, reveals the modulation from the BPF and 2BPF, while BPF comes always with a higher amplitude than 2BPF. Here, all spectra under healthy conditions exhibit lower amplitude cyclic components that are related to the rotor-stator instability pressure pulsations (RF, BPF and their harmonics) that modulate the rotating flow [1], [34]–[36]. It should be noted that those amplitudes are lower in the case of coherence, where the correlation values are normalized against the signal's power and the presence of the latter is less evident. Also, the cavitation spectra of Fig. 16 are similar or of one order of magnitude higher compared to these of the healthy conditions, while in Fig. 15 this difference was much larger and clearer. In other words, the use of higher computational cost methods, such as the CSCor and CSCoh, does not improve the estimation of the healthy and fully cavitation spectra. Furthermore, the comparison of the SES (Fig. 16b) and the EES (Fig. 16c) coherence-based spectra confirms the conclusion that the later will always result in higher values. The same conclusion is drawn from the comparison of  $SES_{CSCor}$  and  $EES_{CSCor}$ , but the spectrum of the latter is not presented for brevity reasons. The aforementioned observations can be critical when it comes to indicators formed based on the different cyclic amplitudes (see Section 3.3), since a stronger amplitude or a difference between the healthy and cavitating conditions amplitudes could result in a better performance of the detection indicators.



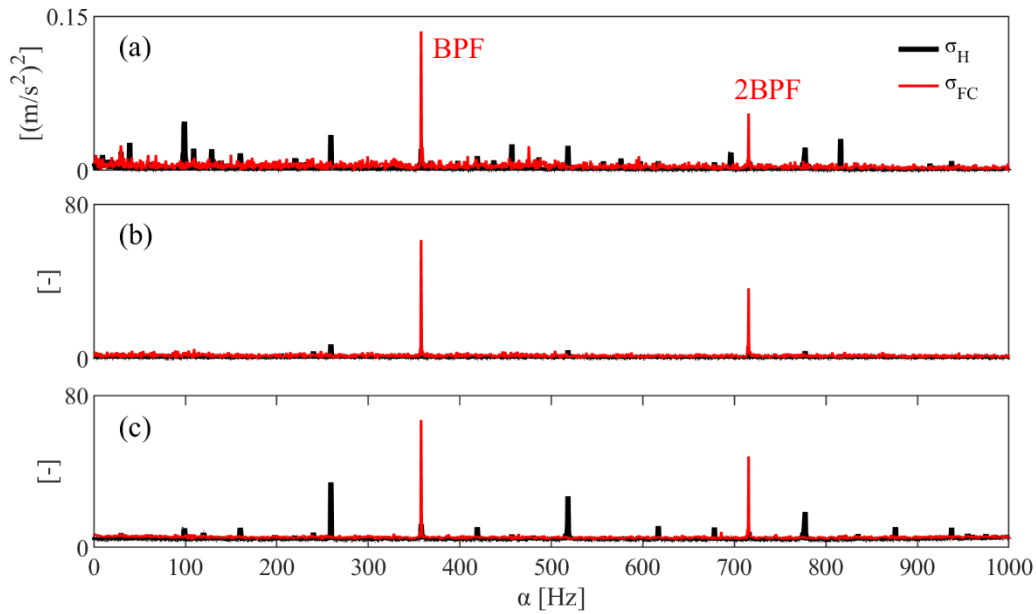


**Figure 16** (a)  $SES_{CSCor}$ , (b)  $SES_{CSCoh}$  and (c)  $EES_{CSCoh}$  for impeller No.2 at  $\Phi=0.046$  at healthy and cavitating conditions.

*Influence of the flowrate*

The previous subsection examined the spectra that correspond to the healthy and fully cavitating conditions at the minimum flowrate of the pump. In order to investigate the effect of the flowrate increase, the results of  $SES$ ,  $SES_{FK}$ ,  $SES_{CSCor}$  and  $SES_{CSCoh}$  from impeller No.2 operating at  $\Phi=0.076$  are shown in Fig. 17. The EES are not shown since they follow similar trend with the  $SES_{CSCor}$  and  $SES_{CSCoh}$  but with slightly higher values and do not provide further insights. The healthy and cavitating conditions correspond to  $\sigma_H=0.78$  and  $\sigma_{FC}=0.16$ , respectively.

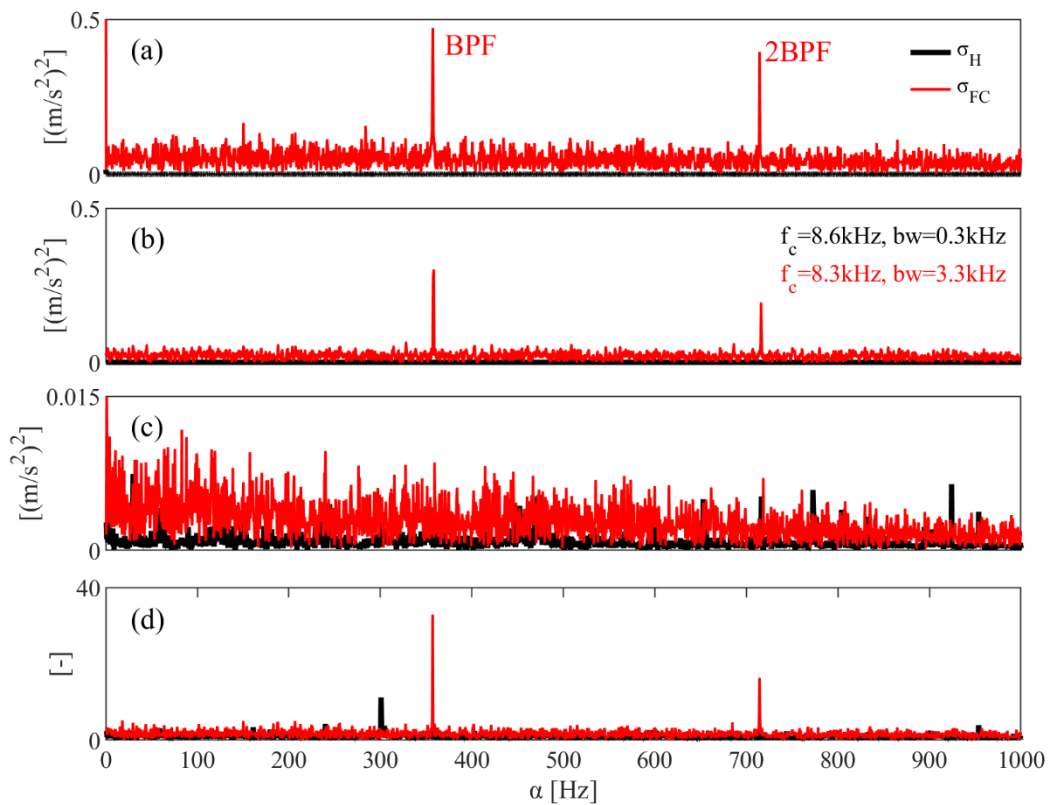


**Figure 17** (a)  $SES$ , (b)  $SES_{FK}$ , (c)  $SES_{CSCor}$  and (d)  $SES_{CSCoh}$  for impeller No.2 at  $\Phi=0.076$  at healthy and cavitating conditions.

The cyclic spectra of  $SES$ ,  $SES_{FK}$  and  $SES_{CSCoh}$  highlight the same dominant modulations under  $\sigma_{FC}$  with the minimum flowrate case, i.e. the BPF and its second harmonic. Under healthy conditions, the spectra do not exhibit components of significant amplitudes, except from the coherence plot (Fig. 17d), where the tenth harmonic of the rotational speed is observed. Also, similarly to what was observed and discussed in Figs. 15 and 16, the modulation amplitude decreases from the use of the FK band pass filter, while the filter characteristics calculated for  $\sigma_{FC}$  are the same. On the other hand, a systematic decrease in the modulations amplitude is clear to all of the three spectra when flowrate increases. More specifically, BPF value drops from 7 to 0.5  $(m/s^2)^2$ , from 2.5 to 0.3  $(m/s^2)^2$  and from 60 to 30 for  $SES$ ,  $SES_{FK}$  and  $SES_{CSCoh}$ , respectively. The main reason for this trend is the lower incidence angle of operation that improves the pump's efficiency and minimizes the secondary flows in the pump and consequently drives it to  $\sigma_{FC}$  that are higher for  $\Phi=0.076$  than  $\Phi=0.046$  [20].

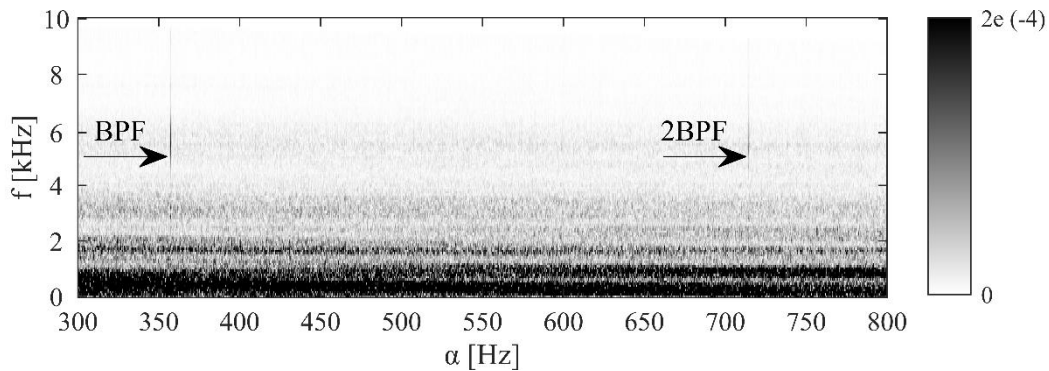


**Figure 18** CSCor for impeller No.2 at  $\Phi=0.076$  and  $\sigma_{FC}=0.16$ .

In Fig. 17c, the  $SES_{CSCor}$  spectrum consists of low amplitude values without clear modulations in contrast with the rest spectra of Figs. 17 and Fig. 16a. In order to further investigate this behavior the CSCor map is given for these operating conditions at Fig. 18. As it can be seen, the correlation values between the cyclic BPF and 2BPF components and the frequency carriers at [5-7] kHz are also there and although their value drops one order of magnitude they can still be distinguished in the plot. However, in this case and contrary to Fig. 10b those correlations values are lower than those estimated for the frequencies  $<1$  kHz for all cyclic components and when integrated in Fig. 17c they do not form significant peaks. Consequently, the effect of the improved angle incidence at higher flow conditions is also indicated at this point. However, this issue is overcome if the correlation result is normalized with the power spectrum value as it can be seen in Fig. 17d, i.e. those low frequency carriers behave similarly to what discussed in Fig. 10. The comparison between the results of Figs. 17c,d highlights once more the higher sensitivity of coherence to peak detection. An alternative to correlation normalization is the calculation of the IES that integrates part of the carriers (Section 2.2) and is presented in Fig. 19. The result now depicts clearly the modulations, while the type of integration selected does not significantly influence the values estimated for IES, as has already been discussed.

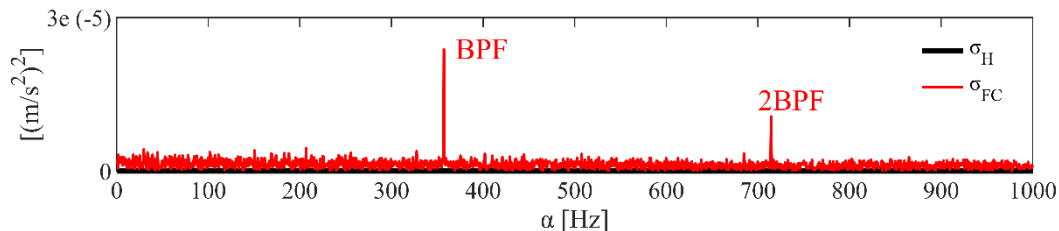


**Figure 19**  $IES_{CSCor-SES}$  for impeller No.2 at  $\Phi=0.076$  and  $\sigma_{FC}=0.16$ .

### Influence of the suction conditions

After investigating how load change influences the cyclic spectra under cavitating conditions, the focus turns to investigating changes in the suction conditions. More specifically, up to this point the conditions discussed corresponded to the minimum  $\sigma$  value tested for each flowrate. At this point, the impeller and load conditions remain the same (No. 2 &  $\Phi=0.076$ , respectively), but the suction pressure increases to the point that corresponds to the visual inception of the vapor bubbles, i.e. at  $\sigma_{VI}=0.58$  (Fig. 5). At this operating condition the impeller operates with a small number of vapor bubbles developed at the leading edge of the suction side of the blade (Fig. 6) and although the bubble collapse cannot really harm the solid surfaces, it is still important to investigate whether a successful detection can be achieved. Thus, the SES,  $SES_{FK}$ ,  $SES_{CSCor}$  and the  $SES_{CSCoh}$  are presented in Fig. 20 so as to check their behavior under  $\sigma_{VI}$ .

The cyclic spectra here exhibit significant differences compare to  $\sigma_{FC}$ , since none of them presents a clear modulation from the BPF. More specifically, the SES (Fig. 20a) depicts the modulation of the signal from the shaft rotation (RF) and its 4<sup>th</sup> and 8<sup>th</sup> harmonic, while the  $SES_{FK}$  (Fig. 20b) does not exhibit any peaks. The latter behavior is related with the small bandwidth of the filter calculated from the FK (800 Hz) that can result in a noisy cyclic spectrum after the implementation of the Hilbert Transform. Similar with the SES, the  $SES_{CSCor}$  (Fig. 20c), exhibits the RF with some harmonics along with the 2BPF, however after observing the coherence based SES (Fig. 20d) it should be concluded that those peaks (both in SES and  $SES_{CSCor}$ ) are possibly not related with cavitation since they disappear after dividing with the power spectrum.

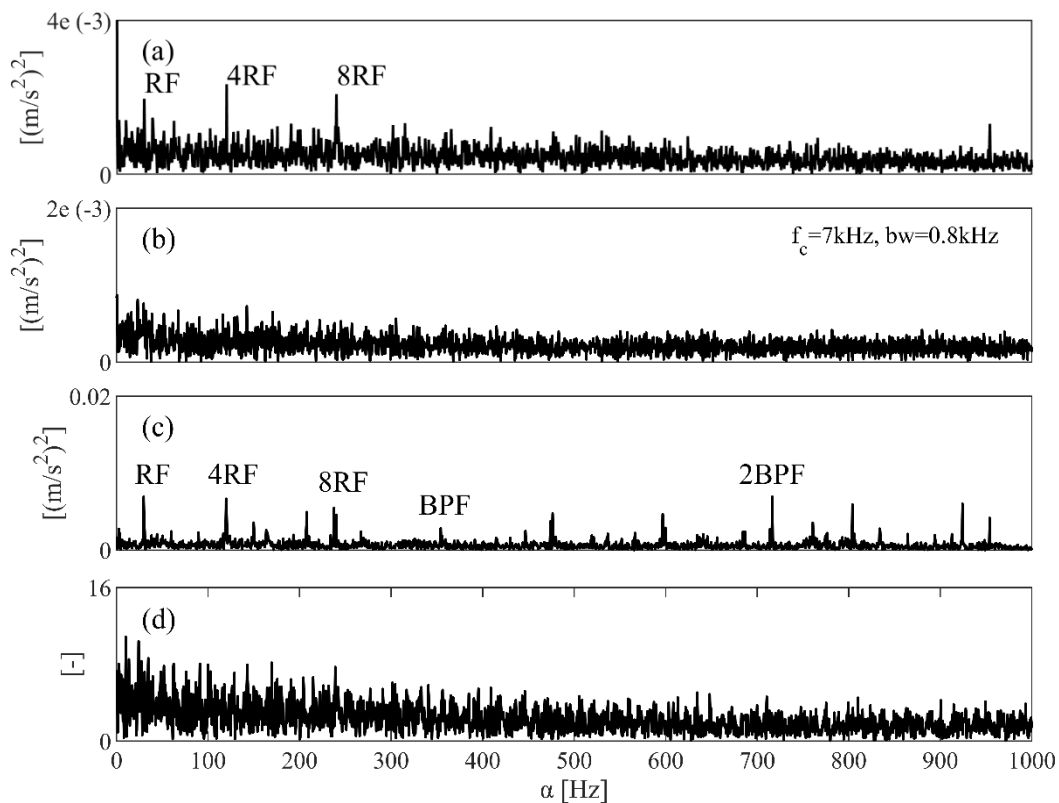


**Figure 20** (a) SES, (b)  $SES_{FK}$ , (c)  $SES_{CSCor}$  and (d)  $SES_{CSCoh}$  for impeller No.2 at  $\Phi=0.076$  at  $\sigma_{VI}=0.58$ .

An interesting observation is made in the  $SES_{CSCoh}$  plot that it doesn't exhibit any clear modulations. As discussed already, no matter the flow conditions (single or two-phase), the vibration signal (flow noise or resonances excited from bubble implosion) is expected to be modulated from RF and BPF, i.e. those peaks should be in the spectrum no matter the operating point discussed. Close to the visual onset, the presence of cavitation in the flow is very dynamic and definitely not continuous for all flow passages

between the blades, i.e. there are moments, where some passages have bubbles and some other they don't or moments where the impeller operates without vapor bubbles. In this case the interaction of the impulsive waves and the overall noise flow with the blades decreases and gives a  $SES_{CSCoh}$  without modulating peaks. It should be highlighted that this observation is not the same case as the one discussed in Fig. 18, where the modulations were clear in the high frequency carriers but where hidden after integrating. Here, after inspecting both the CSCor and CSCoh maps it is confirmed that no high correlation or coherence values appear for high frequency carriers. Consequently the calculation of IES results in cyclic spectra with the form of Fig. 20d and are not presented for brevity reasons. Taking into consideration this behavior but also what it has been already presented for  $\sigma_{FC}$  and  $\sigma_H$  it is concluded that the cyclic spectra behavior exhibits the a trend that is strongly related to the suction conditions.

#### *Influence of the impeller geometry*

After presenting the effect of suction conditions on the cyclic spectra calculation, the influence of the use of a different impeller is investigated. The geometrical differences between the two impellers were highlighted in Section 2.1. For the analysis of impeller No.1, the non-dimensional flowrate  $\Phi=0.040$  which is similar with the partial flowrate discussed for impeller No. 2 in Figs. 15 & 16. Considering that the two impellers are of the same outer diameter, rotate at the same speed and operate under similar load conditions, the effect of the splitter blades and the different incidence angle is expected to be highlighted in the cyclic spectra plots. In Fig. 21 the SES,  $SES_{FK}$  and  $SES_{CSCoh}$  are presented under healthy ( $\sigma_H$ ) and fully cavitating conditions ( $\sigma_{FC}$ ).

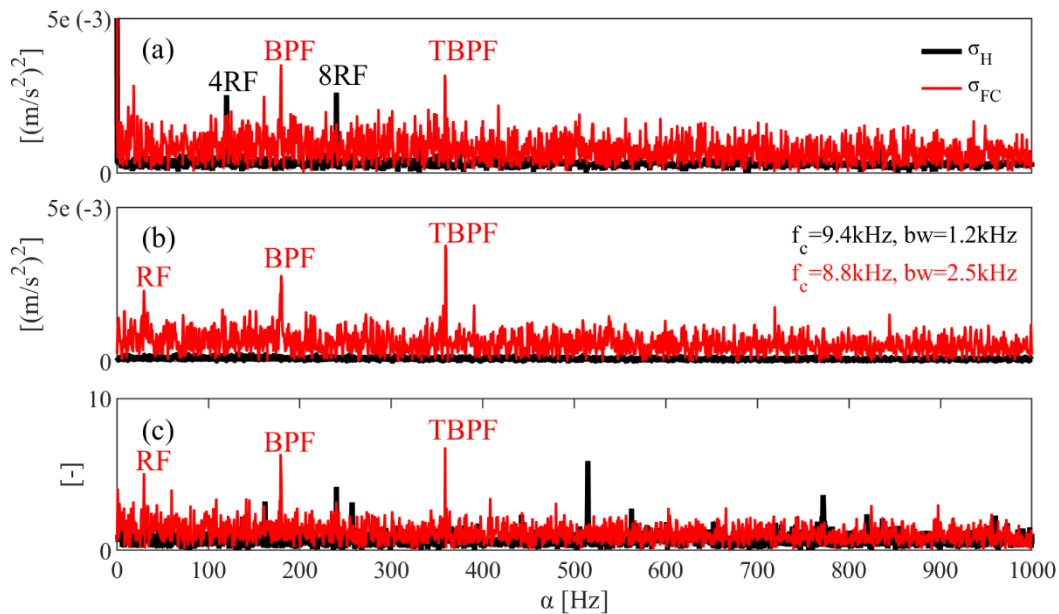


**Figure 21** (a) SES, (b)  $SES_{FK}$ , (c)  $SES_{CSCoh}$  for impeller No.1 at  $\Phi=0.040$  at  $\sigma_H=0.98$  and  $\sigma_{FC}=0.11$ .

Similar to what it is shown for impeller No.2 at Figs. 15 & 16b, at  $\sigma_{FC}$  all of the spectra highlight again clear modulations from the blade related frequencies, while at  $\sigma_H$  amplitude are lower and the harmonics of the shaft periodicities appear. However, in the case of impeller No. 1, the modulation peak of the main blades (BPF) appears together with this of the sum of the splitter and the main blades (TBPF) and in some cases ( $SES_{FK}$  &  $SES_{CSCoh}$ ) a smaller peak at the shaft frequency is also observed. This observation highlights the modulation of both blades types (main and splitter) of the impeller on the imploding vapor bubbles. Also, it is noted that for all the plots of Fig. 21, the amplitude value is lower compared to these of impeller No.2, which are estimated based on the same algorithmic procedure. The smaller amplitudes depict the positive influence of the splitter blades and the lower incidence to the intensity of cavitation in impeller No.1. More specifically, the increased flow path area, as a consequence from the decrease of the number of main blades decelerates the flow and increases the local static pressure conditions, while the improved blade angle design reduces the recirculation and

consequently the local static pressure drops. This observation reveals the difficulty to develop common thresholds and modulation amplitude references when it comes to cavitation monitoring in closed hydraulic turbomachinery. For instance, an amplitude value that for the SES of impeller No. 2 corresponds to heavy cavitating conditions, could correspond to healthy conditions for impeller No. 1. Thus, the indicators that are formed in Section 3.3 are also evaluated, among others, with respect to their applicability in both impellers.

Moreover, from the examination of the SES and  $SES_{FK}$  plots of Fig. 21, it is noticed that the modulation amplitudes of the latter is larger than this of the simple HT application, unlike with the results of impeller No.2 (Figs. 15 & 17). In the case of the impeller with the improved flow conditions (No. 1) the use of the FK and the application of the band pass filter enhances the modulation appearance and does not remove useful information. The latter is one more indication that the increased pressure pulsations resulted from the passing of the blades, regardless they result from the poor pump design or its operation away from its Best Efficiency Point (BEP), makes the modulations clearer and the detection an easier task. It should be also noted that the changes at the filter characteristic after cavitation development follow the same trend with impeller No. 1, i.e. the central frequency drops  $<9$  kHz, while the bandwidth increases to  $>2$  kHz.

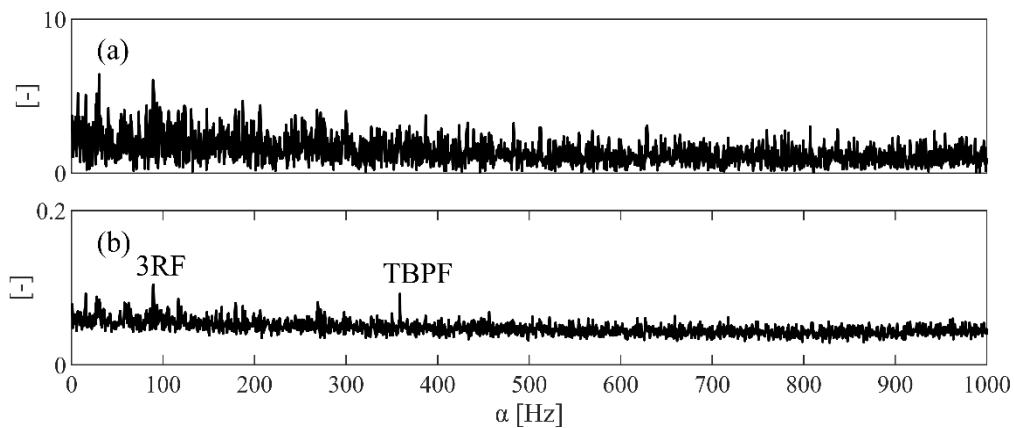


**Figure 22** (a)  $SES_{CSCoh}$  and (b)  $IES_{CSCor-EES}$  for impeller No.1 at  $\Phi=0.040$  at  $\sigma_{VI}=0.40$ .

Finally, the cyclic spectra are also investigated under visual onset conditions and exhibit the same pattern discussed in Fig. 20, i.e. they do not exhibit any clear modulating peaks (Fig. 22). The only exception is for the IES calculated based on EES equation on CSCor map, where during the onset a peak at the TBPF appears. This is an interesting result, since it proves that the modulations expected on the cyclic spectra due to cavitation are less related with the number of blades (the main blades in this case) that exhibit the phenomenon and are mainly related with the main fluid flow excitation, i.e. the pressure pulsations created from all the rotating blades. This can be proved clearly in the case of impeller No. 1 for  $\Phi=0.040$  and  $\sigma_{VI}=0.40$ , since the bubbles appear only at the suction side of the main blades, since the leading edge of the splitter blades is located at bigger diameters, where the energy of the flow has already been increased from the main blades (Fig. 6). However, the modulation presented in Fig. 22b is not the BPF but the TBPF.

### 3.3 Health indicators results and evaluation

After the estimation of the various cyclic spectra, the indicators based on the amplitude of different modulation combinations are calculated and evaluated, according to Section 2.3. The indicators are categorized with respect to the equation that estimates the cyclic spectrum, i.e. (i) the Hilbert-based indicators (black colour in Fig. 23), (ii) the Cyclic Spectral Correlation-based indicators (blue colour), and (iii) the Cyclic Spectral Coherence-based indicators (red colour). Moreover, in this section, the indicators that need the bandwidth either of the band pass filter ( $SES_{FK}$ -based indicators) or of the integration (IES-based indicators) are plotted in empty circles and squares. In order to give an overview of the performance of the indicators, the Evaluation Score 1 (ES1) that is introduced in Section 2.3, is

averaged for all operating conditions examined in each impeller and is presented for all the indicators developed based on different modulating amplitudes (660 for impeller No.1 and 165 for impeller No.2) in Fig. 23. The x-axis indicator No. corresponds to a discrete amplitude or to a sum of discrete amplitude values, presented in detail in Tables 3 and 4 of Section 2.3.

The results of Fig. 23 are very important because they give a clear indication on the families of indicators that are able to efficiently detect cavitation for a wide range of flowrate and suction pressure conditions and more importantly the main observations made do not change when the impeller geometry changes. More specifically, for both impellers, the indicators based on SES,  $SES_f$ ,  $SES_{FK}$ ,  $IES_{CSCor-SES}$  and  $IES_{CSCor-EES}$  exhibit a clearly higher averaged  $ES1$  ( $>0.85$ ) compared to those that either use the total carrier frequency range of CSCor map ( $<0.65$ ) or the CSCoh-based indicators ( $<0.85$ ). The only exception is  $IES_{CSCoh-EES}$ -based indicator No.2 for impeller No.1, which corresponds to the discrete BPF and exhibits  $ES1_{ave}=0.88$  and is higher than the SES-based indicators No.3 (TBPF) and No.4 (2TBPF). For all the other cases, the differentiation in the efficiency of the indicators is clear and observable for both impellers, no matter the combination of the modulating amplitude selected.

Moreover, for the indicators with  $ES1_{ave} >0.85$ , the  $ES1_{ave}$  deviates with respect to the amplitude selection (x-axis) much less compared to the indicators with  $ES1_{ave} <0.85$ . This manifests that those indicators do not only give the minimum number of false alarms and missed detections for all the NPSH, flowrates and impellers tested but also that selection of the amplitude(s) that form the indicator influences less its ability to detect the phenomenon. It is important to note that the  $IES_{CSCor}$ -based indicators are systematically higher than the SES-based indicators, which justifies the use of CSCor estimation towards the revealing of the cavitation related modulations in the pump. However, it should be highlighted that the SES and  $SES_{FK}$ -based indicators do not need any additional user-defined inputs for the determination of the most useful bandwidths and still detect efficiently the phenomenon. Another interesting observation is that the  $ES1_{ave}$  value for SES is higher than this of  $SES_{FK}$  for the impeller No.2, where due to the geometrical characteristics of the impeller the detection is easier. The opposite behavior is observed for impeller No.1. Last but not least, from the results of both impellers it is clear that the value of the indicators with the highest  $ES1_{ave}$  values (SES,  $SES_f$ ,  $SES_{FK}$ ,  $IES_{CSCor-SES}$ ,  $IES_{CSCor-EES}$ ) does not change significantly with the amplitudes that are selected to be summed for their calculation. As expected, the inclusion of more discrete modulating amplitude components results in an even smaller deviation of the  $ES1_{ave}$  value calculated.

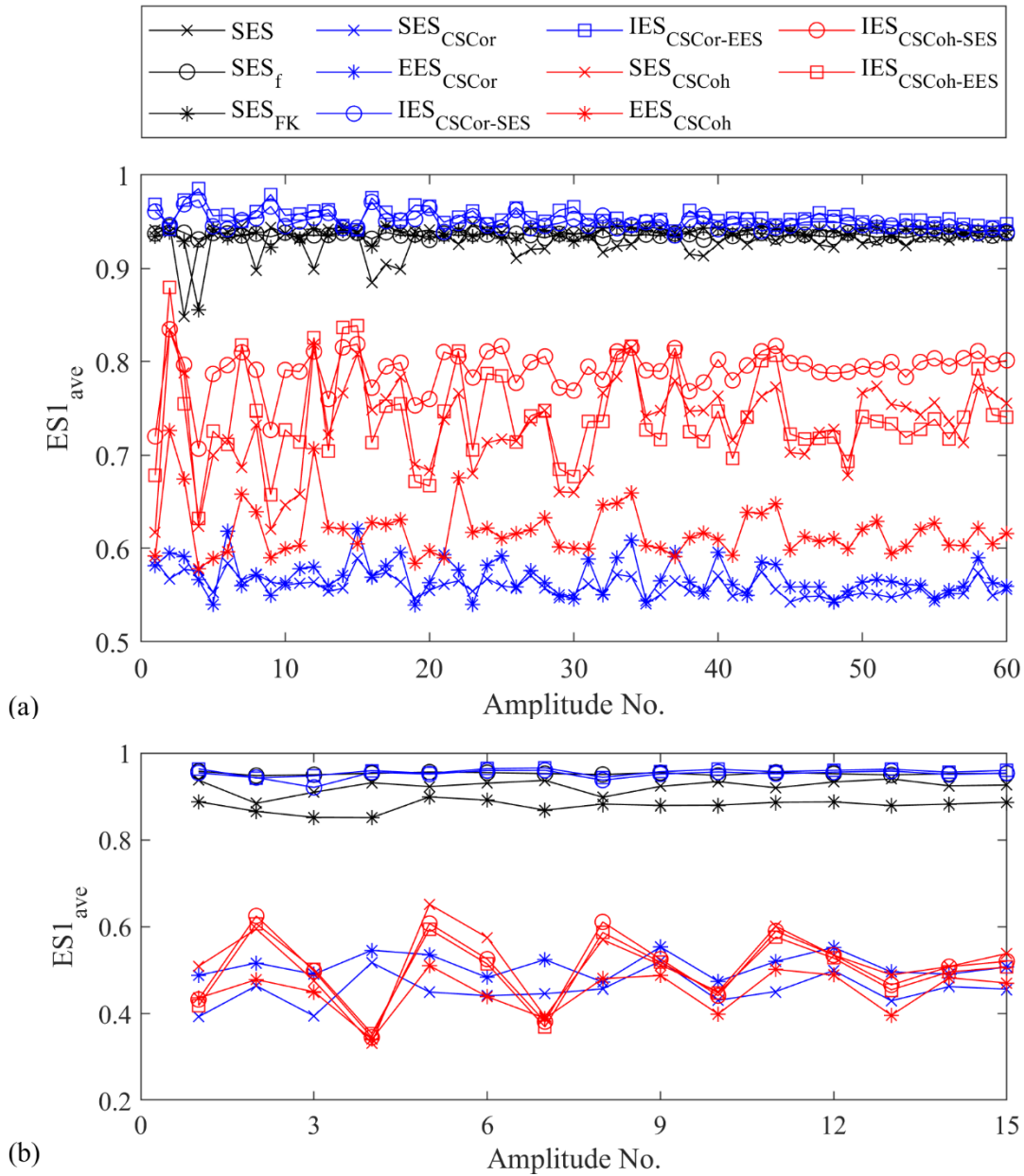


**Figure 23** Averaged ES1 for all indicators of impeller **(a)** No.1, and **(b)** No.2.

In order to depict the differences discussed for ES1 on the indicators plots as a function of suction pressure conditions ( $\sigma$ ), two indicators are selected and plotted in Fig. 24. The indicator of Fig. 24a is based on  $EES_{CSCoh}$  and exhibits  $ES1=0.79$ , while this of Fig. 24b is based on  $IES_{CSCor-EES}$  with  $ES1=0.94$ . In Fig. 24c, the zoomed in plot for Fig. 24b is given in order to highlight the behavior of the indicator relative to the threshold. For both plots, the indicator is calculated based on the sum of RF and TBPF amplitudes, which corresponds to No.8 of Table 3 and Fig. 23a. In both plots, the threshold value that is calculated based on Eq. 21, is drawn with a red dashed value, while the indicator values that correspond to the visual inception point are shown with blue markers. In addition, for each  $\sigma$  condition, the result of the 15 signals that each has 2 seconds duration is presented. Based on the latter, the robustness of the each indicator is evaluated from Eq. 24.

According to the results of Figs. 24a,b the  $EES_{CSCoh}$ -based indicator does not exhibit significant differences between the various  $\sigma$  values. When the pump operates under healthy single-phase ( $\sigma > 0.4$ ) conditions, its value is lower than the threshold (28.4), however after the phenomenon initiation a big

part of the points calculated lie below the threshold resulting in many missed detection and a decrease on the ES1. On the other hand, the  $IES_{CSCor-EES}$ -based indicator exhibits a clear increase on its values after the phenomenon initiation which results in zero missed detections. The  $ES1=0.94 < 1$  in this case results, from 9 points that correspond to healthy conditions ( $\sigma > 0.4$ ) and exhibit higher values from the threshold (Fig. 24c). It should be also noted that the majority of those points correspond to  $\sigma=0.43$ , which is the point exactly before the visual inception of the phenomenon. Under such conditions, it is possible that few bubbles can be created and imploded in a very fast and dynamic way that cannot be followed from the camera system used, however they are possible to increase the value of the  $IES_{CSCor-EES}$ -based indicator.

Finally, a last interesting observation from the plots of Fig. 24 is the differences in the dispersion behavior between the two indicators. On the one hand, the  $EES_{CSCoh}$ -based indicator (Fig. 24a) ranges in the same order of magnitude no matter the  $\sigma$  condition, while on the other hand the  $IES_{CSCor-EES}$ -based indicator (Fig. 24b,c) exhibits a significant increase only after the phenomenon initiation. The small dispersion of this indicator is also clear in the plot of Fig. 24c, where under healthy conditions the values that the indicator takes remain unchanged. The latter observed differentiation is purely the result of the signal processing approach and not of the input signal, which is the same for the results discussed and compared in Fig. 24. As discussed in Section 2.3, this behavior is associated with the robustness of the indicators, i.e. the level of dispersion for the same operating condition that is further discussed in this section.

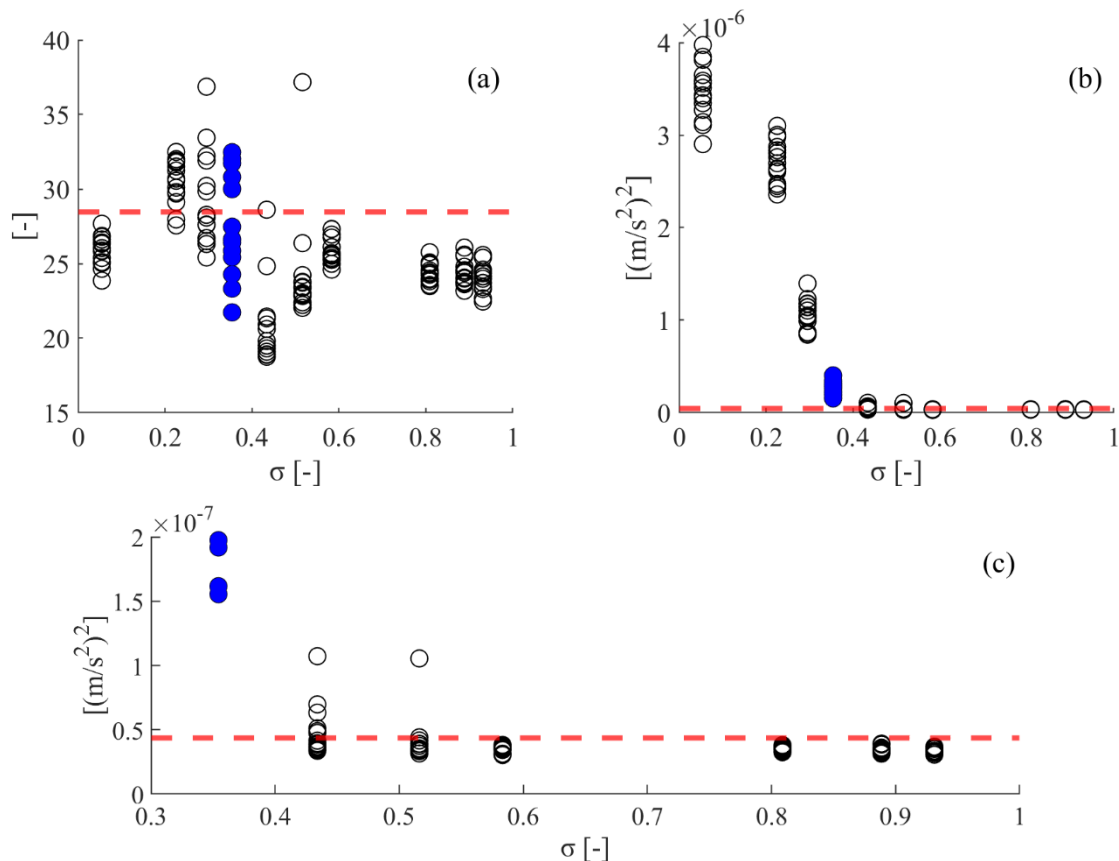
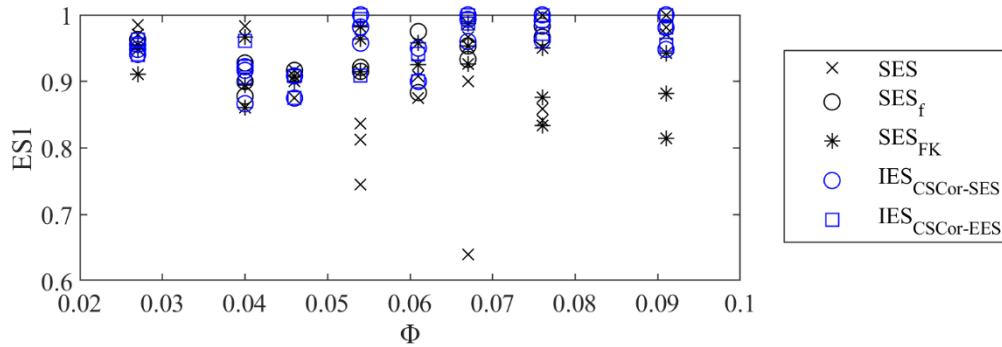


**Figure 24** (a)  $EES_{CSCoh}$ , and (b)  $IES_{CSCor-EES}$ -based indicator amplitudes (Amplitude No.8: RF & TBPF) as a function of  $\sigma$  for impeller No.1,  $\Phi=0.027$ . (c) Zoom in  $IES_{CSCor-EES}$  to highlight the performance close to the threshold (red dashed line).

From the results of Fig. 23, it is concluded that five out of the eleven signal processing methodologies that are used in order to estimate the cyclic spectra and form detection indicators, exhibit systematically higher ES1 for both impellers tested and for this reason the remaining analysis will focus to them. The next step of the analysis is to observe the behaviour of the ES1 in the three different repeatable tests for

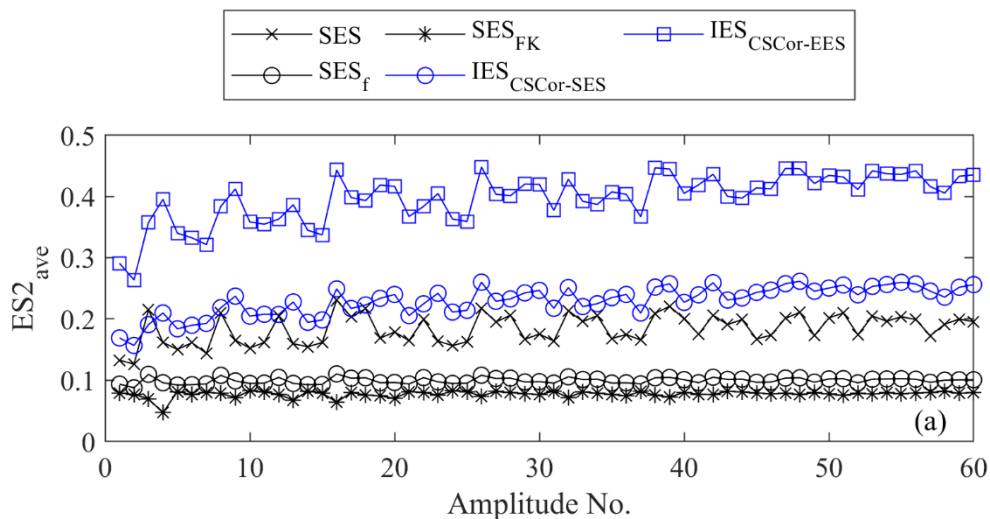


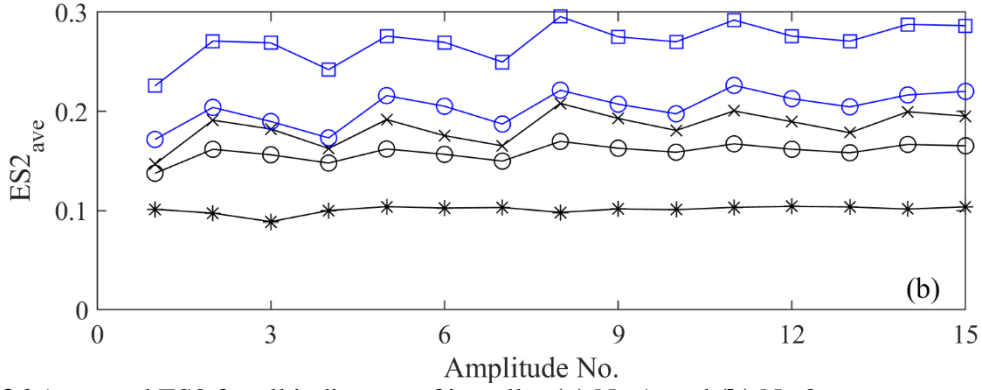
the four flowrates examined per impeller. Similarly to Fig. 24, the indicator formed from the modulating amplitudes of the shaft and the blade passing frequency (TBPF and BPF for impeller No.1 and 2, respectively) is also used at this point. As it is shown in Fig. 23, the  $ES1_{ave}$  results do not change significantly with the amplitudes selected for the formation of the indicator, thus only one is used again in order to reduce the plot complexity. Also, since the non-dimensional flowrate values  $\Phi$  are different for both impellers tested, it is selected to plot the ES1 value as a function of flowrate for both impellers in the same plot, presented in Fig. 25. The averaging of the ES1 values in Fig. 25 results to the values presented for indicators No. 8 and 5 for impellers No.1 (Fig. 23a) and 2 (Fig. 23b), respectively.



**Figure 25** ES1 deviation between the different tests performed in four flowrates ( $\Phi$ ) per impeller.

The ES1 results of Fig. 25 depict that the indicators formed by targeting the high frequency carriers bandwidth ( $SES_f$ ,  $IES_{CSCor-SES}$ ,  $IES_{CSCor-EES}$ ) exhibit small differentiations no matter the flowrate and impeller examined. In the high flowrate cases, where the machine operates closer to the optimum flow conditions, the IES-based indicators reach values  $ES1 \sim 1$ . Also, the ES1 results of those indicators are repeatable when applied to the data of the three tests for each flowrate. On the other hand, the SES and  $SES_{FK}$  indicators, which are formed based on the same input raw data, exhibit less repeatability, especially in the case of  $\Phi=0.054$ ,  $\Phi=0.067$ ,  $\Phi=0.076$  and  $\Phi=0.091$ . Moreover, the latter behavior influences the deviation of the ES1 values in the different flowrates, which is larger compare to the first group of indicators discussed.

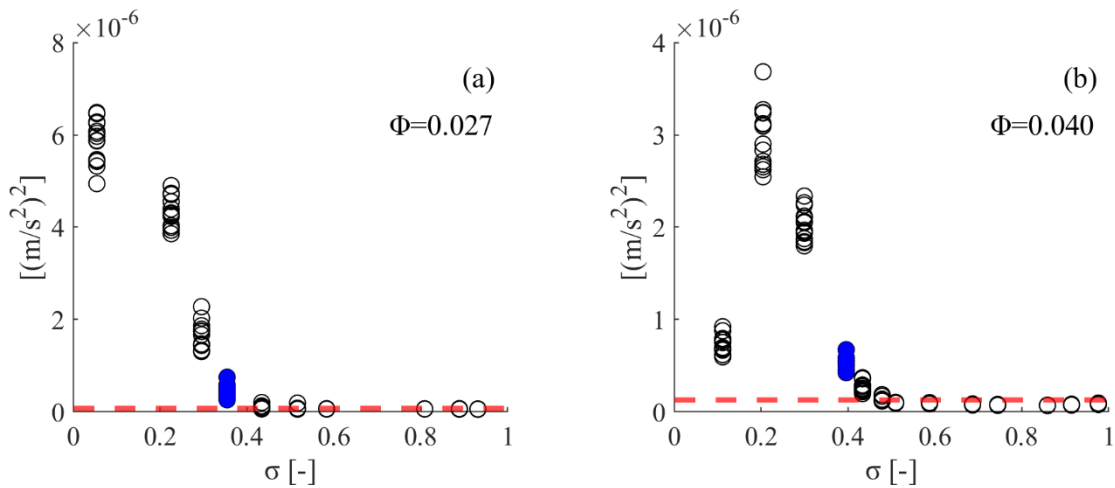




**Figure 26** Averaged ES2 for all indicators of impeller **(a)** No.1, and **(b)** No.2.

The indicators' evaluation ends with the discussion of the  $ES2_{ave}$  results that characterize the indicators' variability in each operating condition, as described in Section 2.3 and Eqs. 23 and 24. Similarly to Fig. 23, the results are averaged for each indicator, and presented, only for the indicators with that exhibit high ES1, in Fig. 26. It is interesting that the  $ES2_{ave}$  results exhibit the same qualitative trend between the two impellers tested. More specifically, the highest  $ES2_{ave}$ , no matter the amplitudes used for the calculation, is exhibited from  $IES_{CSCor-EES}$ -based indicators. Considering that the same indicator has the highest ES1 score for both impellers, both evaluation scores used in this study converge to the conclusion; the  $IES_{CSCor-EES}$ -based indicators give the lowest number of missed detections and false alarms and in parallel, among the most efficient indicators, are the most robust, since their amplitude exhibits the minimum deviation for constant operating conditions. The second highest score is from  $IES_{CSCor-SES}$ , while the Hilbert-based indicators follow. For the latter, the selection of the amplitudes that form the indicator does not influence significantly the result, however for the  $IES_{CSCor-EES}$  the inclusion of more discrete modulating components clearly improves it.

After the discussion and the evaluation on the results of the different indicators presented in this work, this section closes with the presentation of one of the  $IES_{CSCor-EES}$ -based indicators that exhibited high  $ES1_{ave}$  ( $>0.95$ ) for all suction pressure and flowrate condition of both impellers tested. The particular indicator selected includes the use of the shaft and blade passing frequencies along with the second harmonic of the latter. The aim here is to provide a detailed overview of the indicator behavior, discusses the advantages but also highlights the limitation and the possible directions for further improvement in future. The results for impellers No.1 and 2 are shown in Figs. 27 and 28, respectively. Similarly to Fig. 24, the indicator amplitude is plotted against suction conditions, the blue markers correspond to the visual onset and the red line to the MAD threshold calculated from the healthy conditions. In Fig. 28, the plots are accompanied from the zoomed area in order to further highlight the indicators performance close to the threshold.



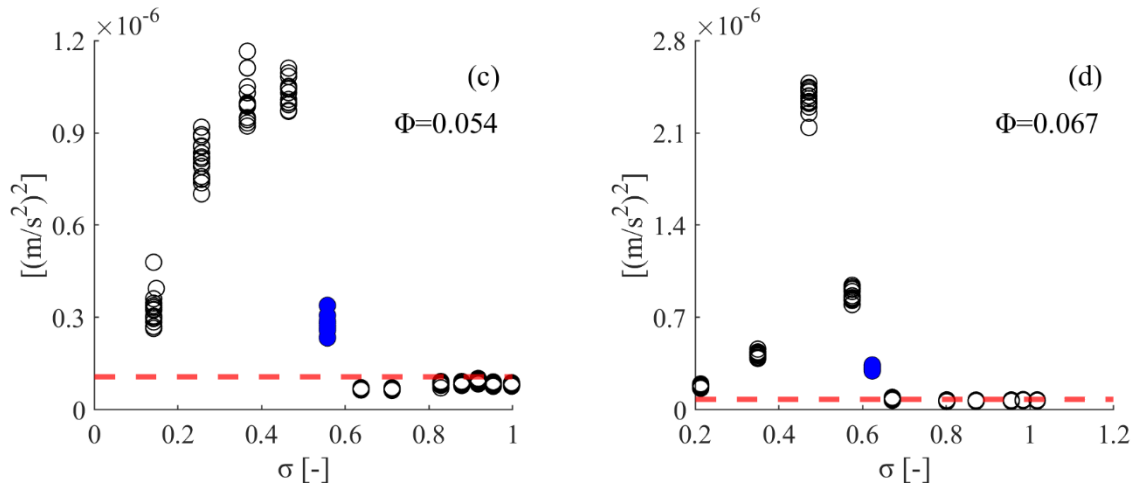


**Figure 27**  $IES_{CSCor-EES}$  indicator with Amplitude No.42 (RF+BPF+TBPF+2TBPF) in different  $\sigma$  for all flowrates of impeller No.1.

The results of both impellers present a clear differentiation between the healthy and cavitating conditions, where the vast majority of the visual onset points lie above the threshold minimizing the number of missed detections. Few false alarms exist in some flowrates (Figs. 27b, 28a,c,d), however most of them correspond to suction pressure conditions close to the visual onset, where it is possible that vapor bubbles exist but not captured from the camera. This behavior confirms the selection made in the Section 2.3 of this article to define different thresholds at different flowrate conditions so as to take into account the load changes on the machines vibration response. In addition, the indicator amplitude remains very similar for all healthy tests of the same flowrate condition, while this trend changes after the cavitation initiation. Moreover, an interesting observation from the results of Figs. 27 and 28 is the increase of the indicator value variability after the initiation of the phenomenon. This is clear to all results presented, no matter the geometry or flowrate tested and for all cases the differentiation is clear from the visual onset point. Moreover, it is clear that the value level of the indicator is correlated with the indicator variability, where the higher is the indicator value the higher is the range noticed. This characteristic can be used also as an indication of the cavitation initiation, improving the detection especially close to the early stages of the phenomenon development. Last but not least, from the plots of both impellers it is shown that the indicator amplitude trend as a function of the suction conditions and consequently of the extent of the phenomenon, is not monotonic. More specifically, in some cases (Figs. 27b-d, 28d) the clear increase in the indicator due to the phenomenon initiation, reaches a local maximum and then drops again to values that lie over the threshold. This behavior is identified in other works that exploit the information of the frequency spectrum and it is caused from the dampening of the vibration signal from the steady cavitation cloud formed under heavy cavitating conditions and lies between the implosions of the newly formed cavities and the sensor. The same trend apparently is exhibited in the case of cyclic frequency-based indicators of the present study.

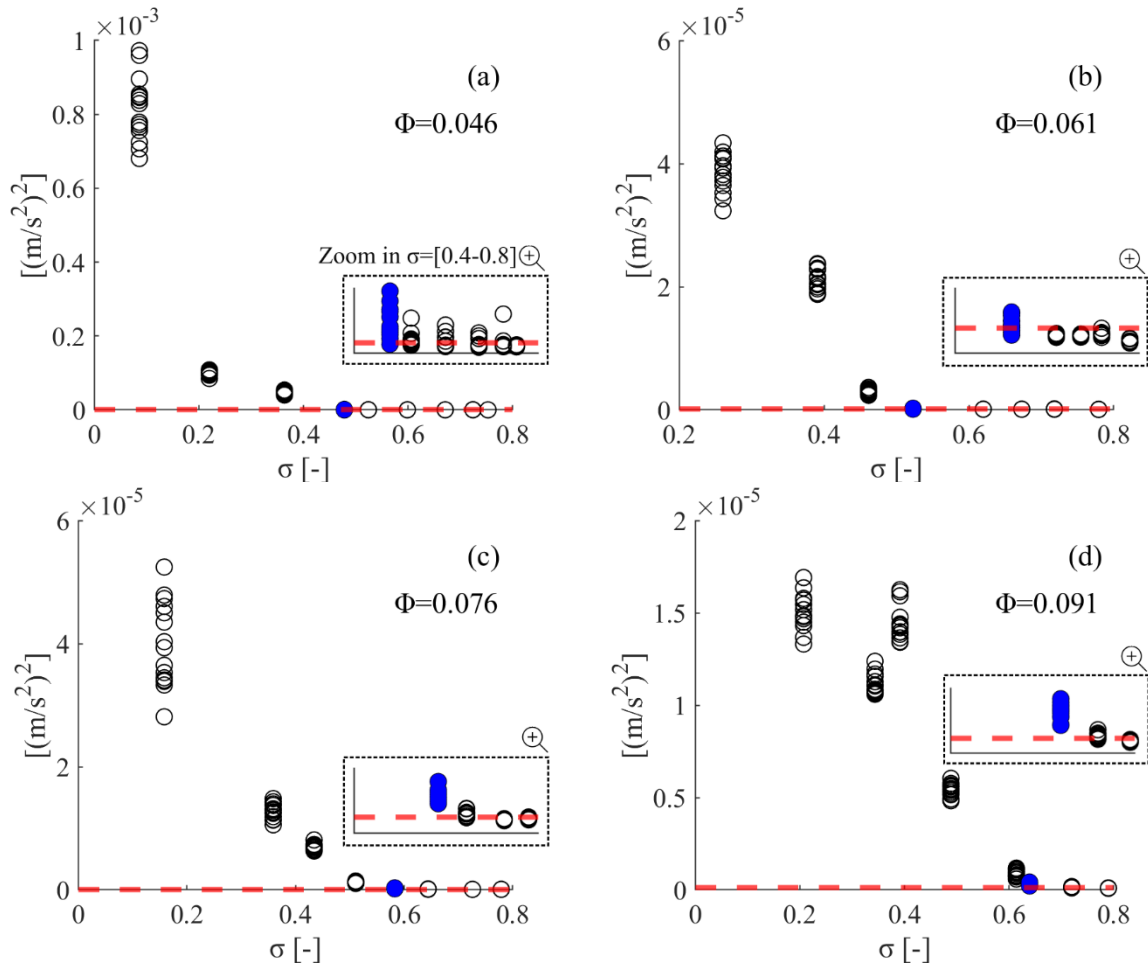


**Figure 28**  $IES_{CSCor-EES}$  indicator with Amplitude No.11 (RF+BPF+2BPF) in different  $\sigma$  for all flowrates of impeller No.2.

## 4. Conclusions

This work examines the effectiveness of different signal processing methodologies that aim to detect cavitation in the cyclic spectrum with the use of flow modulations. Two impellers, in different flowrate and suction pressure conditions are tested in order to investigate the influence of machine geometry, load and cavitation intensity. The onset of the phenomenon is identified from the visual data acquired from a camera that monitors the flow conditions in the rotating impeller. The analysis of the signal processing results starts at the level of the maps and cyclic spectra and continues by evaluating the performance of indicators formed based on cyclic spectra characteristic frequency amplitudes over the different conditions tested. The main conclusions of this work are summarized below.

Starting with the CSCor, CSCoh and FK maps, their result reveal the clear interaction of the fault mechanism with the machine structure and more specifically the fact that bubble implosions excite the high frequency machine resonances. It should be noted that the CSCor and CSCoh maps include more information useful for the engineers and machine users since they reveal the additional interaction of the fault mechanism (bubble implosions) and its symptom on the machine structure (resonance excitation) with the flow field developed in the machine, which in the case of close hydraulic turbomachinery is the pressure pulsations from rotor stator interaction.

At the level of envelope spectra, for extreme cavitating conditions, the BPF modulations on the structural resonances excited from cavitation are clear and can be differentiated without the implementation of computationally heavy demodulation approaches, such as CSCor and FK but by simply using the HT estimation. However, cavitation detection at onset or intermediate stages of

development and in flowrates with improved flow conditions, such as those closer to the BEP, becomes more complicated and the use of more advanced tools (CSCor, CSCoh, FK etc.) in such cases is necessary. No matter the signal processing approach used, modulation amplitudes decrease when flowrate closer to the BEP are tested or in the case of impellers with improved blade angles, since the pressure pulsations become less dominant over the flow field. The main modulation observed in all cases examined in this work is the BPF.

From the evaluation of the indicators with the use of ES1 it is concluded that the SES, SES<sub>f</sub>, SES<sub>FK</sub>, IES<sub>CSCor-SES</sub> and IES<sub>CSCor-EES</sub> approaches are superior since they exhibit the minimum number of false alarms and miss detections for all conditions tested. Additionally, the indicators formed by the high frequency carriers (SES<sub>f</sub>, IES<sub>CSCor-SES</sub>, IES<sub>CSCor-EES</sub>) exhibit higher ES1 values and in some cases where detection is challenging (i.e. close to BEP), the IES-based indicators reach values close to 1. From the ES2 results, it is concluded that IES<sub>CSCor-EES</sub> gives systematically the lowest dispersion value. However, it should be noted that more work should be done towards developing indicators that can describe the extent of the phenomenon and exhibit monotonic trends with the decrease of NPSH values. This can be achieved by optimizing the IES integration range or by removing the pressure pulsations modulations and carriers from all signals before processing them. The aforementioned are parts of the future steps of this work.

## References

- [1] J. Friedrich Gülich, *Centrifugal Pumps*. Springer, 2010.
- [2] I. J. Karassik *et al.*, *Pump handbook*. McGraw-Hill, 2008.
- [3] Y. M. Ganushchak, E. P. J. Körver, and J. G. Maessen, “Is there a ‘safe’ suction pressure in the venous line of extracorporeal circulation system?,” *Perfusion (United Kingdom)*, vol. 35, no. 6, pp. 521–528, Sep. 2020, doi: 10.1177/0267659120936453.
- [4] S. E. Hosseini and A. Keshmiri, “Experimental and numerical investigation of different geometrical parameters in a centrifugal blood pump,” *Research on Biomedical Engineering*, vol. 38, no. 2, pp. 423–437, Jun. 2022, doi: 10.1007/s42600-021-00195-8.
- [5] G. Mousmoulis, J. Anagnostopoulos, and D. Papantonis, “A review of experimental detection methods of cavitation in centrifugal pumps and inducers,” *International Journal of Fluid Machinery and Systems*, vol. 12, no. 1. Turbomachinery Society of Japan, pp. 71–88, 2019. doi: 10.5293/IJFMS.2019.12.1.071.
- [6] Al-Hashmi Salem. A., “Statistical analysis of vibration signals for cavitation detection,” in *IEEE Symposium on Industrial Electronics & Applications*, 2009.
- [7] S. Duplaa, O. Coutier-Delgosha, A. Dazin, O. Roussette, G. Bois, and G. Caignaert, “Experimental study of a cavitating centrifugal pump during fast startups,” *Journal of Fluids Engineering, Transactions of the ASME*, vol. 132, no. 2, pp. 0213011–02130112, Feb. 2010, doi: 10.1115/1.4000845.
- [8] H. Schmidt *et al.*, “Influence of the vibro-acoustic sensor position on cavitation detection in a Kaplan turbine,” *IOP Conf Ser Earth Environ Sci*, vol. 22, no. 5, p. 052006, Mar. 2014, doi: 10.1088/1755-1315/22/5/052006.
- [9] J. Cernetič, J. Prezelj, and M. Čudina, “Use of noise and vibration signal for detection and monitoring of cavitation in kinetic pumps,” in *Acoustics*, Paris, 2008, pp. 2199–2204.
- [10] M. Čudina and J. Prezelj, “Detection of cavitation in situ operation of kinetic pumps: Effect of cavitation on the characteristic discrete frequency component,” *Applied Acoustics*, vol. 70, no. 9, pp. 1175–1182, Sep. 2009, doi: 10.1016/j.apacoust.2009.04.001.

- [11] S. N. Ganeriwala and V. Kanakasabai, "Using vibration signatures analysis to detect cavitation in centrifugal pumps," in *Conference Proceedings of the Society for Experimental Mechanics Series*, Springer New York LLC, 2011, pp. 499–507. doi: 10.1007/978-1-4419-9428-8\_41.
- [12] N. Zhang, M. Yang, B. Gao, and Z. Li, "Vibration characteristics induced by cavitation in a centrifugal pump with slope volute," *Shock and Vibration*, vol. 2015, no., pp. 1–11, 2015, Accessed: Jun. 02, 2022. [Online]. Available: Shock and Vibration
- [13] A. M. Abdulaziz and A. Kotb, "Detection of pump cavitation by vibration signature," *Australian Journal of Mechanical Engineering*, vol. 15, no. 2, pp. 103–110, May 2017, doi: 10.1080/14484846.2015.1093261.
- [14] J. Lu *et al.*, "Detection of the flow state for a centrifugal pump based on vibration," *Energies (Basel)*, vol. 12, no. 16, Aug. 2019, doi: 10.3390/en12163066.
- [15] X. Escaler, E. Egusquiza, M. Farhat, and F. Avellan, "Vibration cavitation detection using onboard measurements," in *Fifth International Symposium on Cavitation*, Osaka, 2003, pp. 1–7.
- [16] X. Escaler, E. Egusquiza, M. Farhat, and F. Avellan, "Cavitation Erosion Prediction in Hydro Turbines from Onboard Vibrations," in *22nd IAHR Symposium on Hydraulic Machinery and Systems*, Stockholm, 2004, pp. 1–10. [Online]. Available: <https://www.researchgate.net/publication/37424346>
- [17] J. H. Lee, J. M. Han, H. G. Park, and J. S. Seo, "Application of signal processing techniques to the detection of tip vortex cavitation noise in marine propeller," *Journal of Hydrodynamics*, vol. 25, no. 3, pp. 440–449, Jul. 2013, doi: 10.1016/S1001-6058(11)60383-2.
- [18] Z. Jiang, K. Sujarittam, B. I. Yildiz, R. J. Dickinson, and J. J. Choi, "Passive Cavitation Detection with a Needle Hydrophone Array," *IEEE Trans Ultrason Ferroelectr Freq Control*, vol. 69, no. 1, pp. 233–240, Jan. 2022, doi: 10.1109/TUFFC.2021.3120263.
- [19] S. Lu, P. Zheng, Y. Liu, Z. Cao, H. Yang, and Q. Wang, "Sound-aided vibration weak signal enhancement for bearing fault detection by using adaptive stochastic resonance," *J Sound Vib*, vol. 449, pp. 18–29, Jun. 2019, doi: 10.1016/j.jsv.2019.02.028.
- [20] G. Mousmoulis, N. Karlsen-Davies, G. Aggidis, I. Anagnostopoulos, and D. Papantonis, "Experimental analysis of cavitation in a centrifugal pump using acoustic emission, vibration measurements and flow visualization," *European Journal of Mechanics, B/Fluids*, vol. 75, pp. 300–311, May 2019, doi: 10.1016/j.euromechflu.2018.10.015.
- [21] L. Xiao, J. Tang, X. Zhang, and T. Xia, "Weak fault detection in rotating machineries by using vibrational resonance and coupled varying-stable nonlinear systems," *J Sound Vib*, vol. 478, Jul. 2020, doi: 10.1016/j.jsv.2020.115355.
- [22] G. Mousmoulis, C. Yiakopoulos, G. Aggidis, I. Antoniadis, and I. Anagnostopoulos, "Application of Spectral Kurtosis on vibration signals for the detection of cavitation in centrifugal pumps," *Applied Acoustics*, vol. 182, Nov. 2021, doi: 10.1016/j.apacoust.2021.108289.
- [23] S. Lawrence Marple, "Computing the discrete-time analytic signal via fft," *IEEE Transactions on Signal Processing*, vol. 47, no. 9, pp. 2600–2603, Sep. 1999, doi: 10.1109/78.782222.
- [24] M. Feldman, *Hilbert Transform Applications in Mechanical Vibration*. Wiley, 2011. doi: 10.1002/9781119991656.
- [25] X. Escaler, E. Egusquiza, T. Mebarki, F. Avellan, and M. Farhat, "Field assessment of cavitation detection in hydropower plants," in *Proceedings of the XXIst IAHR Symposium on Hydraulic Machinery and Systems*, 2002, pp. 1–8.
- [26] P. Bourdon, R. Simoneau, and J.-M. Oorey, "Accelerometer and pit counting detection of cavitation erosion on a laboratory jet and a large Francis Turbine," in *XVII IAHR Symposium*, 1994.

- [27] C. Nicolet, A. Zobeiri, P. Maruzewski, and F. Avellan, "Experimental Investigations on Upper Part Load Vortex Rope Pressure Fluctuations in Francis Turbine Draft Tube," *International Journal of Fluid Machinery and Systems*, vol. 4, no. 1, pp. 179–190, Mar. 2011, doi: 10.5293/ijfms.2011.4.1.179.
- [28] J. Antoni, "Fast computation of the kurtogram for the detection of transient faults," *Mech Syst Signal Process*, vol. 21, no. 1, pp. 108–124, Jan. 2007, doi: 10.1016/J.YMSSP.2005.12.002.
- [29] A. Moshrefzadeh and A. Fasana, "The Autogram: An effective approach for selecting the optimal demodulation band in rolling element bearings diagnosis," *Mech Syst Signal Process*, vol. 105, pp. 294–318, May 2018, doi: 10.1016/j.ymssp.2017.12.009.
- [30] K. Wu, N. Chu, D. Wu, and J. Antoni, "The Enkrogram: A characteristic frequency extraction method for fluid machinery based on multi-band demodulation strategy," *Mech Syst Signal Process*, vol. 155, Jun. 2021, doi: 10.1016/j.ymssp.2020.107564.
- [31] W. A. Smith, Z. Fan, Z. Peng, H. Li, and R. B. Randall, "Optimised Spectral Kurtosis for bearing diagnostics under electromagnetic interference," *Mech Syst Signal Process*, vol. 75, pp. 371–394, Jun. 2016, doi: 10.1016/j.ymssp.2015.12.034.
- [32] J. H. Lee and J. S. Seo, "Application of spectral kurtosis to the detection of tip vortex cavitation noise in marine propeller," *Mech Syst Signal Process*, vol. 40, no. 1, pp. 222–236, Oct. 2013, doi: 10.1016/j.ymssp.2013.04.002.
- [33] H. S. Han, C. N. Lee, S. H. Jeon, K. H. Lee, and S. H. Park, "Development of an evaluation method to determine cavitation inception speed with aft hull vibration using kurtosis of the DEMON spectrum," *Ocean Engineering*, vol. 152, pp. 167–180, Mar. 2018, doi: 10.1016/j.oceaneng.2018.01.075.
- [34] A. Zobeiri, J.-L. Kueny, M. Farhat, and F. Avellan, "Pump-turbine Rotor-Stator Interactions in Generating Mode: Pressure Fluctuation in Distributor Channel EPFL Ecole polytechnique fédérale de Lausanne Switzerland," 2006.
- [35] C. Nicolet, E. Lausanne, S. C. N. Ch, and N. Ruchonnet, "One-Dimensional Modeling of Rotor Stator Interaction in Francis Pump-Turbine," 2006.
- [36] S. Li, N. Chu, P. Yan, D. Wu, and J. Antoni, "Cyclostationary approach to detect flow-induced effects on vibration signals from centrifugal pumps," *Mech Syst Signal Process*, vol. 114, pp. 275–289, Jan. 2019, doi: 10.1016/j.ymssp.2018.05.027.
- [37] W. A. Gardner, "The Spectral Correlation theory of cyclostationary time-series," 1986.
- [38] W. A. Gardner, "Measurement of Spectral Correlation," *IEEE Trans Acoust*, vol. 34, no. 5, pp. 1111–1123, 1986, doi: 10.1109/TASSP.1986.1164951.
- [39] W. A. Gardner, "Exploitation of Spectral Redundancy in Cyclostationary Signals," *IEEE Signal Process Mag*, vol. 8, no. 2, pp. 14–36, 1991, doi: 10.1109/79.81007.
- [40] R. B. Randall, J. Antoni, and S. Chobsaard, "The relationship between spectral correlation and envelope analysis in the diagnostics of bearing faults and other cyclostationary machine signals," *Mech Syst Signal Process*, vol. 15, no. 5, pp. 945–962, 2001, doi: 10.1006/mssp.2001.1415.
- [41] J. Antoni, "Cyclic spectral analysis of rolling-element bearing signals: Facts and fictions," *J Sound Vib*, vol. 304, no. 3–5, pp. 497–529, Jul. 2007, doi: 10.1016/j.jsv.2007.02.029.
- [42] J. Antoni, G. Xin, and N. Hamzaoui, "Fast computation of the spectral correlation," *Mech Syst Signal Process*, vol. 92, pp. 248–277, Aug. 2017, doi: 10.1016/j.ymssp.2017.01.011.
- [43] P. Borghesani and J. Antoni, "A faster algorithm for the calculation of the fast spectral correlation," *Mech Syst Signal Process*, vol. 111, pp. 113–118, Oct. 2018, doi: 10.1016/j.ymssp.2018.03.059.

- [44] R. Zimroz and W. Bartelmus, "Gearbox Condition Estimation Using Cyclo-Stationary Properties of Vibration Signal," *Key Eng Mater*, vol. 413–414, pp. 471–478, Jun. 2009, doi: 10.4028/www.scientific.net/KEM.413-414.471.
- [45] Mahvash Ali and Lakis A. Aouni, "Application of Cyclic Spectral Analysis in Diagnosis of Bearing Faults in Complex Machinery," *Tribology Transactions*, vol. 58, pp. 1151–1158, 2015.
- [46] J. Wodecki, A. Michalak, R. Zimroz, T. Barszcz, and A. Wyłomańska, "Impulsive source separation using combination of Nonnegative Matrix Factorization of bi-frequency map, spatial denoising and Monte Carlo simulation," *Mech Syst Signal Process*, vol. 127, pp. 89–101, Jul. 2019, doi: 10.1016/j.ymssp.2019.02.052.
- [47] R. L. Marinho and F. A. P. Barúqui, "Cavitation Aggressiveness Estimation in Hydro Turbines Based on Cyclostationary Modeling," *Brazilian Journal of Instrumentation and Control*, vol. 03, no. 01, pp. 1–9, 2015.
- [48] H. Sun, S. Yuan, and Y. Luo, "Cyclic Spectral Analysis of Vibration Signals for Centrifugal Pump Fault Characterization," *IEEE Sens J*, vol. 18, no. 7, pp. 2925–2933, Apr. 2018, doi: 10.1109/JSEN.2018.2804908.
- [49] K. Wu *et al.*, "Cavitation Characterization of Fluid Machinery Based on Cyclostationary Analysis: Part 1—Cavity Type Identification by Carrier Distribution," *J Fluids Eng*, vol. 144, no. 9, Sep. 2022, doi: 10.1115/1.4054290.
- [50] K. Wu *et al.*, "Cavitation Characterization of Fluid Machinery Based on Cyclostationary Analysis: Part 2—Cavity Development Evaluation by Modulation Intensity," *J Fluids Eng*, vol. 144, no. 9, Sep. 2022, doi: 10.1115/1.4054291.
- [51] G. Aggidis, "<https://www.lancaster.ac.uk/engineering/research/energy/>."
- [52] G. Mousmoulis, C. Yiakopoulos, I. Kassanos, I. Antoniadis, and J. Anagnostopoulos, "Vibration and acoustic emission monitoring of a centrifugal pump under cavitating operating conditions," in *IOP Conference Series: Earth and Environmental Science*, Institute of Physics Publishing, Dec. 2019. doi: 10.1088/1755-1315/405/1/012003.
- [53] H. Sun, S. Yuan, and Y. Luo, "Characterization of cavitation and seal damage during pump operation by vibration and motor current signal spectra," *Proceedings of the Institution of Mechanical Engineers, Part A: Journal of Power and Energy*, vol. 233, no. 1, pp. 132–147, Feb. 2019, doi: 10.1177/0957650918769761.
- [54] X. Escaler, E. Egusquiza, M. Farhat, F. Avellan, and M. Coussirat, "Detection of cavitation in hydraulic turbines," *Mech Syst Signal Process*, vol. 20, no. 4, pp. 983–1007, May 2006, doi: 10.1016/j.ymssp.2004.08.006.
- [55] J. H. Lee, "A weighting function for improvement of spectral coherence based envelope spectrum," *Mech Syst Signal Process*, vol. 160, Nov. 2021, doi: 10.1016/j.ymssp.2021.107929.
- [56] J. I. Taylor, *The Vibration Analysis Handbook*, First Edition. 2000.
- [57] Y. Zhifeng, W. Fujun, X. Ruofu, and L. Zhuqing, "Experimental investigation of relationship between pressure fluctuations and vibrations for a double suction centrifugal pump," 2011. [Online]. Available: <http://www.asme.org/about-asme/terms-of-use>
- [58] D. Siegel, J. Lee, and H. Al-Atat, "A Systematic Methodology for Gearbox Health Assessment and Fault Classification," 2011. [Online]. Available: <https://www.researchgate.net/publication/268304492>
- [59] S. T. Kandukuri, A. Klausen, K. H. Van, and K. G. Robbersmyr, "Fault diagnostics of wind turbine electric pitch systems using sensor fusion approach," in *Journal of Physics: Conference Series*, Institute of Physics Publishing, Jun. 2018. doi: 10.1088/1742-6596/1037/3/032036.



- [60] C. Leys, C. Ley, O. Klein, P. Bernard, and L. Licata, "Detecting outliers: Do not use standard deviation around the mean, use absolute deviation around the median," *J Exp Soc Psychol*, vol. 49, no. 4, pp. 764–766, Jul. 2013, doi: 10.1016/j.jesp.2013.03.013.